AN ABSTRACT OF THE THESIS OF

Han-Ting Lin for the degree of Master of Science in Electrical and Computer Engineering presented on March 9, 2020.

Title: Field-Free Precessional Magnetization Switching by Focused Surface Acoustic Waves

Abstract approved:

_____

Albrecht Jander

In this research, the possibility of the precessional magnetization switching by focused surface acoustic waves, without external magnetic field, has been demonstrated. The technique of generating an effective magnetic field by applying stress to a magnetostrictive material via a surface acoustic wave is applied to perform field-free magnetization switching. It is shown that focused interdigital transducers can provide sufficient surface acoustic wave amplitude to achieve switching. For the purpose of controlling the timing and direction of acoustic waves, this research proposes a device containing two perpendicular channels of the interdigital transducers making ±45° angles with the initial magnetization direction of a ferromagnetic thin film at the focal point of the focused interdigital transducers. At first, one of the interdigital transducer channels is excited to generate surface acoustic waves, which will change the magnetization direction in the magnetostrictive material as a consequence of the Villari effect, in combination with precessional magnetization dynamics. Next, the other channel is excited when the magnetization is furthest away from its initial position. This second surface acoustic wave will finalize the magnetization reversal, and thus,

field-free switching can be accomplished. To perform the magnetization switching, a high strain amplitude in the magnetostrictive material is required and hence surface acoustic wave focused interdigital transducers are necessary.

Focused interdigital transducers are design for Y-cut lithium niobate substrate. Due to the crystalline structure of Y-cut lithium niobate, the surface acoustic wave velocity in this material depends on propagation direction. To design focused interdigital transducers that will generate maximum strain amplitude in the magnetostrictive material, the difference between phase velocity and group velocity, as well as the power flow angle, of the acoustic wave on this crystalline structure must be considered. The research design of a surface acoustic wave focused interdigital transducer device has been experimentally verified by laser interferometry. The surface acoustic wave is focused with 400 pm vibrational amplitude at the focal point. Finally, the magnetization dynamics with the experimental strain value has been simulated to demonstrate the possibility of the field-free magnetization switching.

Field-Free Precessional Magnetization Switching by Focused Surface Acoustic Waves

by
Han-Ting Lin

A THESIS

submitted to

Oregon State University

in partial fulfillment of
the requirements for the
degree of

Master of Science

Presented March 9, 2020
Commencement June 2020

Master of Science thesis of Han-Ting Lin presented on March 9, 2020

APPROVED:

Major Professor, representing Electrical and Computer Engineering

Head of the School of Electrical Engineering and Computer Science

Dean of the Graduate School

I understand that my thesis will become part of the permanent collection of Oregon State University libraries. My signature below authorizes release of my thesis to any reader upon request.

Han-Ting Lin, Author

ACKNOWLEDGEMENTS

I would like to thank Dr. Albrecht Jander and Dr. Pallavi Dhagat for guiding me through my research and giving me the opportunity of involving in different projects. It has been my pleasure to learn from you and this lab.

Secondly, I would like to thank those who have served on my committee: Dr. Andreas Weisshaar, and Dr. Leonard Coop. Thank for your time and patience to my thesis and final defense.

To all Applied Magnetics Lab members: Khliad Masood, Nabila Nujhat, Cason Rivard, Andrew Russell, Shane Witsell, Shane Allen and Madeleine Cannamela. Thank you all for helping me on my thesis writing and final presentation.

For the FIDT device, I would like to thank Nabila Nujhat. Thank you for being to spend so much time to fabricate this device; I hope I did not bring you too much trouble.

In the end, I think I should also thank all my friends and my parents for supporting me while studying abroad in the United States. Thank you all.

TABLE OF CONTENTS

TABLE OF CONTENTS (Continued)

Page

LIST OF FIGURES

Figure Page

LIST OF FIGURES (Continued)

Figure Page

LIST OF FIGURES (Continued)

Figure Page

LIST OF FIGURES (Continued)

Figure Page

LIST OF FIGURES (Continued)

Figure Page

LIST OF TABLES

LIST OF SYMBOLS

Symbol	Units	Description
a_x	m	Length of thin film in easy axis
a_y	m	Length of thin film in hard axis
A	m	Vibrational amplitude
$\boldsymbol{B_m}$	T	Inverse magnetostrictive field (flux density)
d	m	Thin film thickness
D_i	m	Initial laser beam diameter
D_m	m	Laser spot diameter
$\boldsymbol{e}$	Unitless	Easy axis direction
E_σ	J/m^3	Free energy density
$f_{reference}$	Hz	Frequency of reference peak
f_{saw}	Hz	Frequency of SAW
$\boldsymbol{H_{bias}}$	A/m	Bias field
$\boldsymbol{H_d}$	A/m	Demagnetization field
$\boldsymbol{H_{eff}}$	A/m	Effective field
$\boldsymbol{H_m}$	A/m	Magnetoelastic field

*Note, bolded symbols represent vectors, and non-bolded symbols represent scalars

LIST OF SYMBOLS (Continued)

Symbol	Units	Description
I	W/m^2	Intensity of laser beam
k	1/m	Wavenumber
K	J/m^3	Uniaxial anisotropy constant
K^2	Unitless	Piezoelectrical coupling constant
l	m	Path length of laser
$\boldsymbol{m}$	Unitless	Unit vector of magnetic moment
$\boldsymbol{M}$	A/m	Magnetic magnetization
$\boldsymbol{M_s}$	A/m	Saturation magnetization
N	Unitless	Demagnetization factor
t	s	Time
u_x	Unitless	Normalized displacement in x-axis
u_z	Unitless	Normalized displacement in z-axis
v_0	m/s	SAW velocity in piezoelectric material
v_g	m/s	Group velocity
v_p	m/s	Phase velocity
w_0	m	Laser focal spot radius
Y	Pa	Young's modulus

*Note, bolded symbols represent vectors, and non-bolded symbols represent scalars

LIST OF SYMBOLS (Continued)

Symbol	Units	Description
γ	Hz/T	Gyromagnetic ratio
ε_s	Unitless	In-plane strain
θ	degree	Angle of phase velocity
θ_d	degree	Angle of diffraction limit
θ_s	degree	Angle between stress and magnetization
Θ	degree	Beam divergence
λ	Unitless	Gilbert damping factor
λ_{laser}	m	Wavelength of laser
λ_s	Unitless	Magnetostriction coefficient
λ_{SAW}	m	Wavelength of SAW
μ_0	H/m	Free space permeability
σ_s	N/m^2	Stress applied to sample
ϕ	rad	Phase of SAW
φ	rad	Phase difference of laser beams
φ_0	rad	Phase offset of laser beams
ψ	degree	Power flow angle
ω_{SAW}	rad/s	Frequency of SAW
ω_{mod}	rad/s	Frequency of AOM

*Note, bolded symbols represent vectors, and non-bolded symbols represent scalars

Chapter 1 Introduction

This thesis proposes a new method of magnetization switching without an external magnetic field using surface acoustic waves (SAWs) for achieving this goal. SAWs provide the strain to the ferromagnetic thin film for creating an *effective* magnetic field that will cause the magnetization switching. For this reason, the ferromagnetic material must be magnetostrictive to convert the strain into an effective field. Magnetostriction along with the SAW will be the driving force for our proposed field-free switching method.

Magnetostriction was first discovered in 1842 by James Joule [1]. Magnetostriction describes the deformation and shape change of a ferromagnetic material as it is being magnetized. This deformation effect is caused by the magnetic domains in a ferromagnetic material rotating and shifting when an external magnetic field is applied. The magnetostriction coefficient (λ_s) is described as the ratio of strain generated in the magnetic material to the change in the magnetization. Based on the understanding of magnetostriction, the inverse magnetostrictive effect can be used for generating effective magnetic fields inside the ferromagnetic material. We will use the inverse magnetostrictive effect, also known as Villari effect explained in chapter 3, as the cornerstone of this research.

1.1 Motivation

The main data storage devices are solid state drives (SSDs) and hard disk drives (HDDs) nowadays. SSDs have the advantage of writing and reading speed compared to HDDs, because HDDs need to spin the disk to the specific position to read or write

a bit and hence the speed depends on the spinning mechanism. Another problem with the HDDs is that it requires an external coil to generate magnetic field to write the data on the magnetic disk. On the other hand, SSDs are expensive than the HDDs in terms of price per data bit. The reason of high cost of SSDs is the memory cells are precisely fabricated at certain location with a complicated logic gate structure. To combine the advantages of HDDs and SSDs, an experimental study on using the magnetic field from a current in the line to write data to magnetic thin-film memory was proposed [2]. However, a coil is still required to generate an external magnetic field to write data. Therefore, the field free magnetization switching in a magnetic material can be used for addressing magnetic memory like SSDs.

Camara's research group proposed a new way to cause field free magnetization switching by acoustic wave in which they demonstrated that it is possible to achieve switching using only acoustic waves [3,4]. Despite this advancement, the conditions of the experiment are undesirable for common applications as the temperature was at 100 K, the temperature for low field resonance in GaAs. Camara's experiment also required large driving powers (32 dBm to 35 dBm) to overcome the long-distance decay of the acoustic wave. The long-distance decay is caused by the magneto-acoustic attenuation of SAW. This large power would be inefficient in modern devices and therefore technologically inefficient.

The purpose of our current research then is to induce field free magnetization switching at room temperature and at a lower driving power than previously achieved. In order to do this, modulating and focusing the SAW is required. To achieve this goal, focused interdigital transducers (FIDTs) were utilized. The FIDTs are created based by

calculating the SAW velocity in different crystalline directions in Lithium Niobate ($LiNbO_3$) crystal and creating finger spacing and curvature to focus the SAW at a central region. For our devices, we have two FIDT channels on an elliptically shaped device allowing for the focusing of two independent high amplitude acoustic waves in two different directions, which is required for field free magnetization switching.

1.2 Thesis Organization

Chapter 2 of this thesis reviews relevant fundamental background knowledge for designing FIDTs and understanding field-free magnetization switching. We introduce basic concepts about the SAW and the SAW transducers. We then introduce the main method, that the SAW vibrational amplitude was measured, the heterodyne laser beam interferometry as well as the function of the interferometer setup that we have been using for this research.

In chapter 3, we discuss the technique and the design of FIDTs device. It outlines the details and concerns required for designing FIDTs on crystalline materials. First, we introduce the benefit of the FIDT compared to a straight IDT and mention some works that have been done before using IDTs. Second, the design method for FIDTs on crystalline materials is covered. The phase velocity of SAWs in Y-cut $LiNbO_3$ and the relationship between slowness curve are important concepts for determining the power flow angle and group velocity. Finally, we determine the design of the FIDTs on our chosen crystalline material, Y-cut $LiNbO_3$.

In chapter 4, we present both the simulation results of the precessional switching and the experimental results of the acoustical vibration of the focused IDTs.

The precessional switching results are generated by MATLAB® program. Also discussed are the acoustic vibrational results taken from the interferometer. In summary, here we present discussion about all the results and the assumptions that we have made for the simulation.

In chapter 5, we summarize the results from the experiments and simulations and conclude the possibility of field-free magnetization switching. In the end, we suggest future steps to improve this research by using different substrate and designing the shape of the magnetostrictive materials.

Chapter 2 Generation and Characterization Surface Acoustic Waves

2.1 Surface Acoustic Wave Interdigital Transducers

A SAW is a type of mechanical strain wave that propagates on a solid surface. SAWs have been widely applied in electronic circuit designs. This technique is based on the elasticity of the piezoelectric material. An IDT is a device that converts an electrical signal to an acoustic signal and vice versa by piezoelectricity. It is widely used in our mobile devices nowadays, because it has some advantages for integrated circuit design. The velocity of the SAW is much smaller than the electromagnetic wave, so the size of a SAW IDT device can be much smaller than a normal electronic circuit operating at the same frequency. A general SAW IDT contains a pair of conductor as electrode and a piezoelectric substrate as shown in figure 2.1.

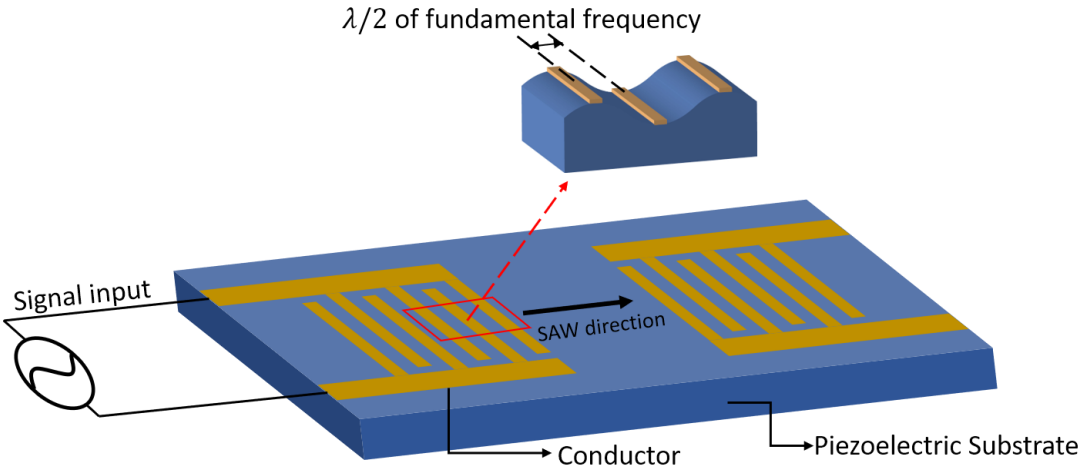

Figure 2.1 Illustration of an IDT for generating surface acoustic wave in plane propagation. The yellow pads indicate the metal electrodes (IDT fingers), and the piezoelectric substrate is shown in blue.

Compression and tension of the substrate surface takes place between the IDT fingers as shown in the cross-section image on the top of figure 2.1. In figure 2.1, the signal input is connected on the left-hand side of the IDTs, and the SAW generated by the

IDT propagates to the right. For the SAW, the mechanism mostly remains on the surface, because the wave amplitude decays exponentially down into the substrate. By switching the voltage of those electrodes from positive voltage to negative voltage, the IDT can generate SAW propagation along the in-plane direction with controlled frequency.

The wavelength of SAW and the velocity of SAW are the key factors to design a SAW IDT device. According to the illustration of figure 2.1 and the acoustic wave velocity of a particular substrate, the spacing between IDT fingers can be determined as half of the SAW wavelength on that substrate. However, the vibrational amplitude generated by straight IDT is not strong enough for the goal of this work. Therefore, a focused IDT device will be introduced that can achieve the requirement of high vibrational amplitude of this research. The focused IDT requires less power to generate the same level of the vibrational amplitude of a straight IDT. This is because it focuses acoustic waves to a certain point by its unique geometry. Therefore, a focused IDT requires less conductor finger pairs than a straight IDT to excite the same level of vibrational amplitude, so the bandwidth of a focused IDT is than a straight IDT. In order to measure the vibrational amplitude due to the SAW, we introduce a laser heterodyne interferometer in the next section.

2.2 Laser Heterodyne Interferometer System

Interferometry uses the phenomenon of wave interference to observe and measure the displacement of vibration dynamically. For imaging SAW, the heterodyne interferometer can observe the phase and the magnitude of the surface acoustic waves

as a function of frequency [5]. The measurement concept of the heterodyne interferometer is modulating the frequency of the laser beams, and applying the technique of heterodyne to modulate the signals by the intensity difference of the two laser beams [6]. A heterodyne interferometer modulates laser beams into two different frequencies. One of the laser beams is a probing beam, while the other is the reference beam. By recombining these two beams and demodulating the signal, results in a vibrational displacement which can be detected by the interferometer [6]. The following figure 2.2 is the schematic of the heterodyne interferometer illustrating the optical path of the laser and other components:

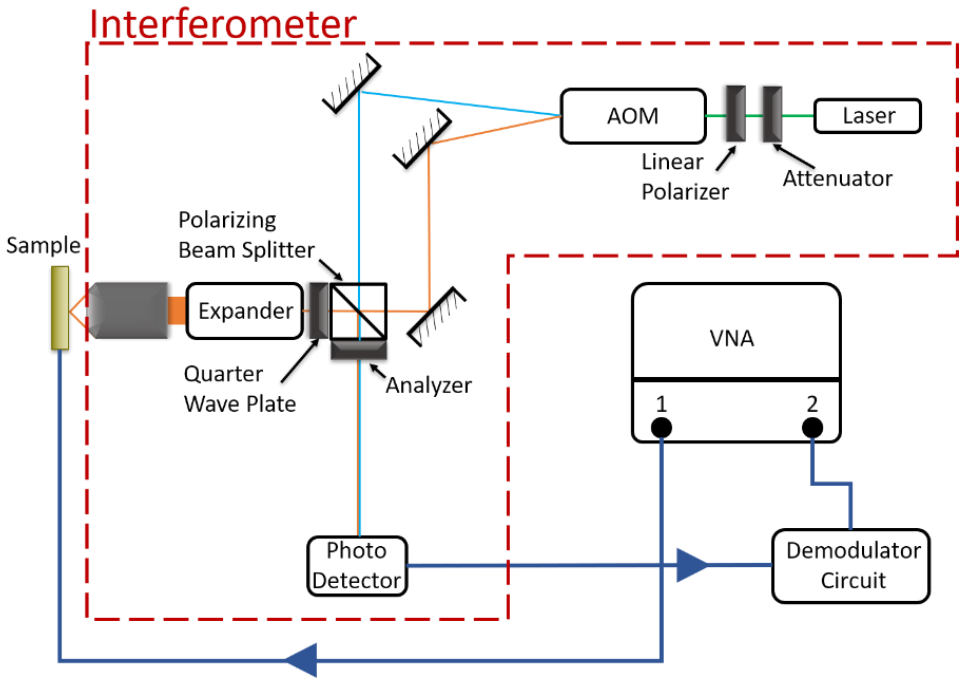

Figure 2.2 Illustration of optical components and electronic analytical devices. Light blue beam is the reference laser beam, orange beam is the probing beam, green line is the original laser beam that is generated by a HeNe laser. (See figure 2.5 for the detail of the demodulator circuit.)

The laser is becomes linearly polarized after passing through the linear polarizer. The purpose of using the linear polarizer is to maximize the laser energy which goes

into the polarizing beamsplitter. A quarter wave plate placed on the side of the probing beam will rotate the polarization of the returning beam by 90 degrees, so that it comes back into the polarizing beamsplitter, while the probing beam can pass to the photo detector without losing energy.

An acousto-optic modulator (AOM) is placed after the linear polarizer in figure 2.2. The AOM modulates one beam into two beams with 200 MHz frequency difference. The light blue line in figure 2.2 is the reference beam, which directly goes into the photo detector. On the other hand, the orange color line represents the sample probing beam. The sample probing beam goes into a 3x beam expander to increase the beam diameter. Therefore, the sample probing beam can be focused to a small area that is enough to measure the SAW vibration with micrometer level wavelength.

2.2.1 Laser Spot Size Calculation

For minimizing the probing laser spot size that shines on the sample, the incident laser diameter must be matched with the back aperture of the focusing lens as much as possible. The laser used in this research is a 5 mW green laser (CrystalLaser CL532-005). According to its data sheet, the initial beam diameter is 0.36 mm and the beam divergence is 2 mrad. The beam diameter before the expander is 3.36 mm, calculated by the definition of the beam divergence, from the following equation [7]:

$$\Theta = atan(\frac{D_m - D_i}{2 \times l}) \tag{2.1}$$

where, Θ is the beam divergence, D_i is the initial beam diameter, l is the path length, and D_m is the laser spot diameter before the expander. After the 3x expander, the spot size becomes ~10 mm. Therefore, the beam diameter is the largest possible before the

lens, and it is small enough to fit in the back aperture of the lens. The focused size on the sample is calculated by the following equation [8]:

$$\theta_d = \frac{D_m}{f} = \frac{\lambda_{laser}}{\pi w_0} \tag{2.2}$$

$$2w_0 = \frac{2f\lambda_{laser}}{\pi D_m} \tag{2.3}$$

In (2.2), θ_d is the angle of diffraction limit, f is the focal length of the objective lens, λ_{laser} represents the wavelength of laser, 532 nm, and w_0 is the radius of the focusing spot. As a result, w_0 is the desired focal spot size, that is determined by (2.3). All these parameters are illustrated in the figure 2.3 below:

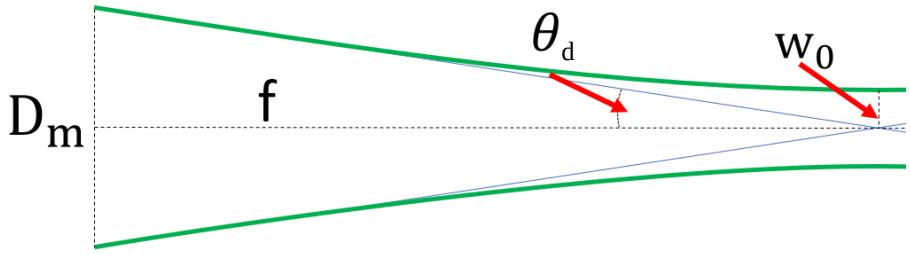

Figure 2.3 Illustration of laser focusing and beam divergence. A laser comes from the left-hand side and passes through an objective lens. The focusing spot is on the right-hand side.

The final goal of this calculation is to get the correct laser spot size for measuring the SAW vibration of the sample. This research uses an 10x lens (Nikon CFI Plan Achromat 10x) as the probing lens for the interferometer setup [9]. The focal length is 20 mm. The laser focusing spot diameter (w_0) of our interferometer setup is 0.67 μm, this number is a calculated result from the (2.3). The sampling spot size should be less than half of the wavelength of the SAW device, which is 3.411 μm for fundamental frequency, and 1.137 μm for the third harmonic. As a result, the laser spot after the lens is small enough for detecting the SAW vibration of the device we designed in this research. The next section will discuss about how the signal that we

detect from the photodetector is processed and how to convert the electrical signal into the vibrational amplitude.

2.2.2 Signal Processing and Vibrational Amplitude

The vector network analyzer (VNA) in figure 2.2 produces an electrical signal from port 1 to excite the SAW device, so the device can vibrate at a certain frequency and power. The probing beam shines on the vibrating SAW device, so that the reflection beam gets modulated with the vibrational frequency of the SAW device. Furthermore, the returning beam from the sample passes into the beamsplitter and redirects to the photodetector. At the photodetector, it recombines with the reference beam. Therefore, the frequency spectrum received, by the photodetector as shown in figure 2.4 below, is where two peaks are modulated by the frequency of SAW and the reference frequency from the AOM, ω_{mod}.

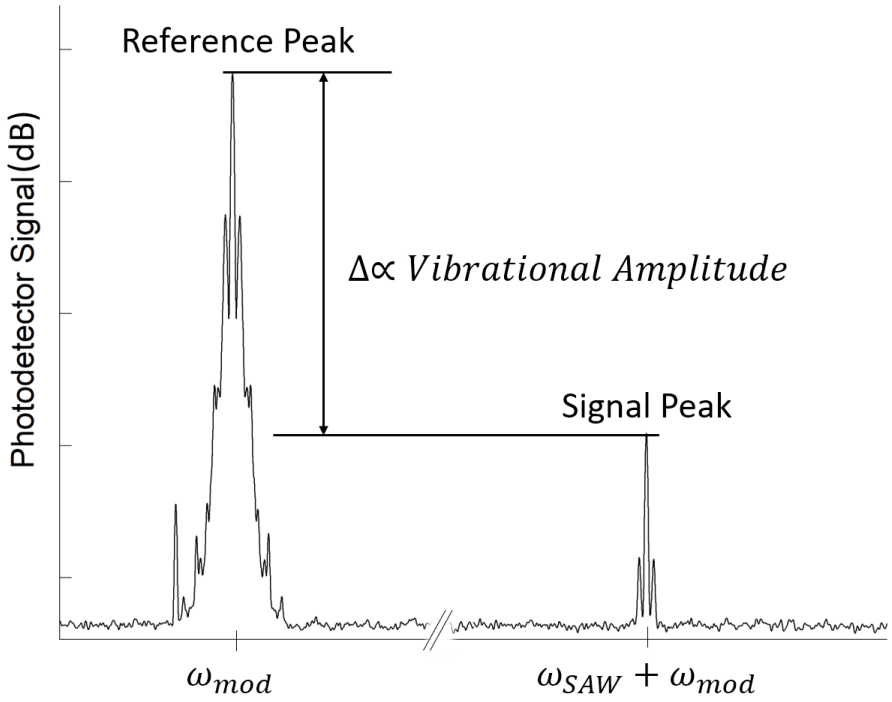

Figure 2.4 Frequency spectrum of the receiving signal from the photodetector, and these peaks are going to be processed by the demodulator circuit.

On the very left side of figure 2.4, the reference peak at ω_{mod} is the carrier frequency given by the AOM, which is 200 MHz in this interferometer setup. ω_{SAW} represents the operating frequency of the SAW device given by VNA port 1. After the probing beam recombines with the reference beam, the receiving frequency spectrum would have two peaks of modulated signal ($\omega_{SAW} - \omega_{mod}$ and $\omega_{SAW} + \omega_{mod}$). However, in the actual measurement, only the upper peak ($\omega_{SAW} + \omega_{mod}$) is detected. Therefore, the upper peak is also called the signal peak, this peak includes the information of vibrational amplitude [6]. Intensity of laser received is:

$$I(t) = I_1 + I_2 + 2\sqrt{I_1 I_2} cos\ (\omega_{mod} t + \varphi(t)) \qquad (2.4)$$

I_1 and I_2 represent the intensity of two beams, and the third term is due to interference between the two beams depending on their phase difference, $\varphi(t)$. $\varphi(t)$ is created by the vibration of the SAW device, so it can be written as:

$$\varphi(t) = \varphi_0 - \frac{4\pi}{\lambda_{laser}} A cos(\omega_{SAW} t + \phi) \tag{2.5}$$

where, λ_{laser} is the wavelength of the laser light, *A* is the vibrational amplitude of the SAW, ϕ is the phase of the SAW, and φ_0 is the phase offset in radius from two beams. φ_0 is caused by the path length difference between two beams.

Finally, after plugging (2.5) into (2.4), the time-varying term of (2.4) can be written as:

$$\begin{aligned} I_{12}(t) = {} & 2\sqrt{I_1 I_2}(\cos(\omega_{mod} t + \varphi_0) \\ & + \frac{2\pi}{\lambda_{laser}} A \sin\{\sin[(\omega_{mod} - \omega_{SAW})t + \varphi_0 - \phi] \\ & + \sin[(\omega_{mod} + \omega_{SAW})t + \varphi_0 - \phi]\}) \end{aligned} \tag{2.6}$$

As a result, the SAW vibrational amplitude (*A*) and phase can be reached by solving (2.6). The vibrational amplitude is proportional to the difference between the reference peak and the signal peak. From (2.6), the reference peak can be represented by the first term, $2\sqrt{I_1 I_2}\cos(\omega_{mod} t + \varphi_0)$, and the signal peak, $2\sqrt{I_1 I_2}\frac{2\pi}{\lambda_{laser}} A sin(\sin[(\omega_{mod} + \omega_{SAW})t + \varphi_0 - \phi])$. The reference peak has magnitude, $2\sqrt{I_1 I_2}$, at ω_{mod}, and signal peak has magnitude, $2\sqrt{I_1 I_2}\frac{2\pi}{\lambda_{laser}} A$, at $\omega_{mod} + \omega_{SAW}$. Therefore, vibrational amplitude can be determined as the ratio, $\frac{\lambda_{laser}}{2\pi}$, times the power difference in decibel between the reference peak and the signal peak.

2.2.3 Demodulator Circuit

The purpose of the demodulator circuit is shifting the signal peak at $\omega_{SAW} + \omega_{mod}$ back to the SAW resonance frequency, ω_{SAW}. The concept of demodulator circuit is similar to a RF heterodyne receiver, but the 200 MHz reference peak is the local oscillator in our case [10]. The RF mixer mixes the signal peak with the 200 MHz reference peak (ω_{mod}), and creates two signals with frequency ω_{SAW} and $\omega_{SAW} + 2\omega_{mod}$. The circuit diagram below shows the detail and every component that is included in the demodulator circuit of our application.

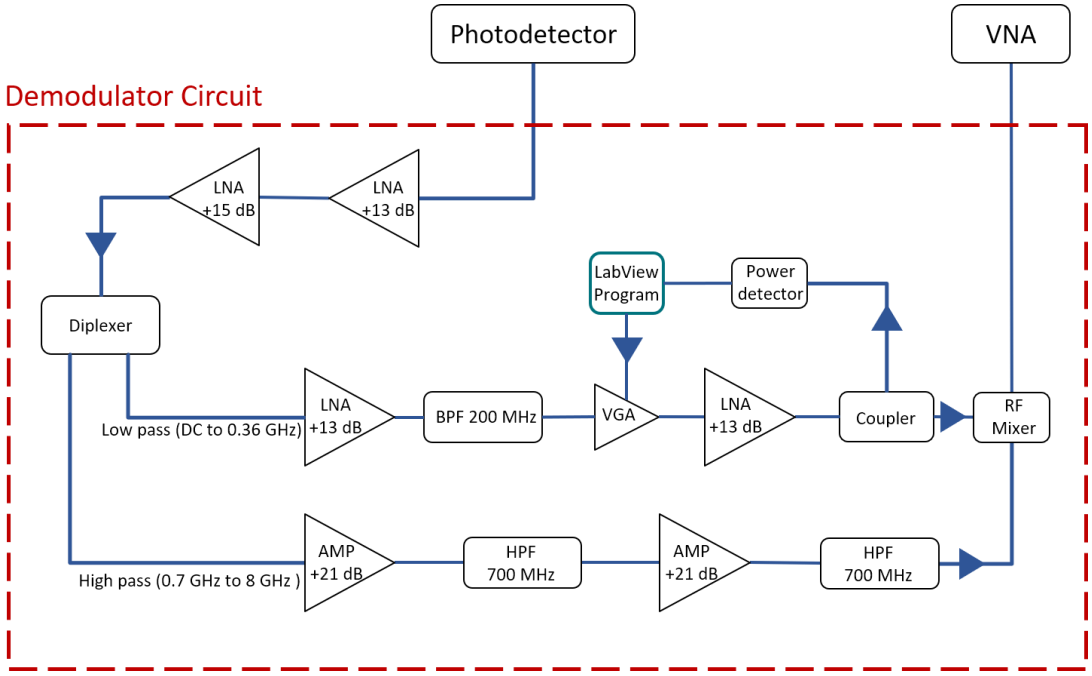

Figure 2.5 The circuit diagram of the demodulator circuit. This circuit demodulates the signal at the $\omega_{SAW} + \omega_{mod}$ to ω_{SAW}, and sends it back to the port 2 of the VNA.

This circuit in after the photodetector received laser signal. Two low noise amplifiers amplify the laser signal that received from photodetector, because the signal peak can be lower than -130 dBm, which is too low for most of the component to operate. The diplexer splits the reference peak and the signal peak, the low-pass port

filters out the frequency between DC to 360 MHz, and the high-pass port filters out the frequency higher than 700 MHz. The RF mixer uses the reference peak as the local oscillator, and the signal peak as the input signal. However, the RF mixer has a minimum power requirement 13 dBm to do the modulation. Therefore, we added a loop with a variable gain amplifier (VGA in figure 2.5) for maintaining the power of the 200 MHz reference peak to 13 dBm. In the VGA loop, the RF coupler couples the output power to the RF mixer and sends a feedback signal to a LabView program for comparing of the power is lower or higher than 13 dBm. Then according to the results of comparison, the program would use the voltage control to fix and maintain the VGA loop output power to 13 dBm.

2.3 Focused Interdigital Transducer in Crystalline Material

The FIDT is widely used in different applications nowadays, such as convolvers [11], RF channelizers [12], and time-Fourier transformers [13] for signal processing. Our application in this research is using the physical displacement that is created by the SAW to generate the effective field for magnetization switching. Through applying stress to the magnetostrictive sample in different directions, the field-free precessional magnetization switching can be implemented. However, a straight SAW IDT is not able to achieve our goal in this application. FIDTs are more functional for creating higher amplitude of the acoustic wave vibration at a focal point. Although designing SAW IDTs has been developed for several years, adapting the IDTs designing concepts on anisotropic materials are still challenging. The first challenge is the anisotropic effect in SAW propagation in crystalline material, so it would cause an angle shift from

the original propagation of SAW. Moreover, the group velocity of SAW propagating in anisotropic material is different from its phase velocity. In order to align the focusing spot at the center of the device, we need to make sure the angle of the curve and the phase equality on every direction. Therefore, the design of FIDT in crystalline structure depends on the SAW propagation angle and velocity in different directions.

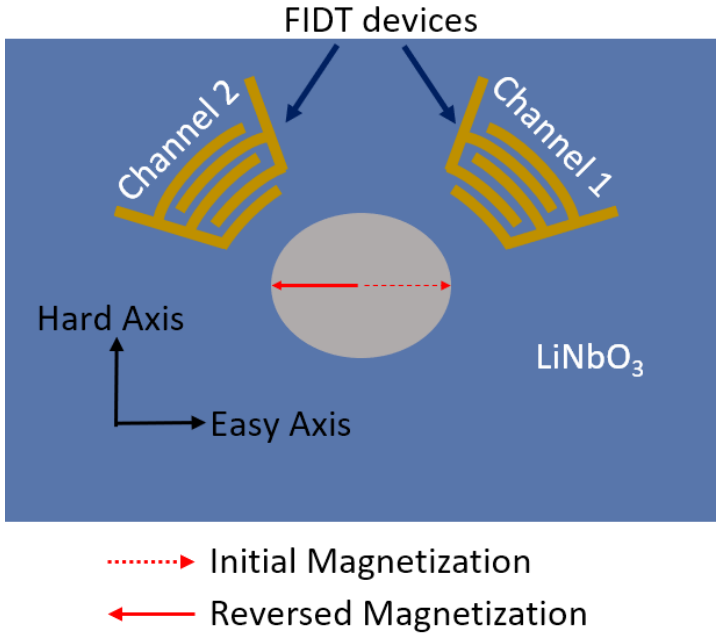

Figure 2.6 Proposed device for field-free precessional switching. By exciting channel 1 and channel 2 consecutively, the magnetization of magnetic material is reversed to the other direction along the easy axis.

The goal of designing and fabricating FIDTs on anisotropic materials is for controlling the magnetostriction in different direction to achieve the field-free precessional magnetization switching. The proposed device of FIDTs is shown in figure 2.6. The FIDT devices can focus the SAWs to the magnetic material, that is placed according to the focal point of the FIDT, so we can change the direction of the magnetic domain at the focal point and reach high intensity of the vibrational amplitude.

In Li's dissertation [14], he applied a similar concept of focusing SAW for increasing the intensity of the vibrational amplitude and he addressed this application to the magnetic recording method, acoustically assisted magnetic recording. To achieve the field-free switching by acoustic wave, it requires at least two directions of the acoustic strain. Therefore, in this work, two channels of FIDTs can reach out two directions of the magnetic domain anisotropy.

In this thesis, Y-cut $LiNbO_3$ wafer was used, because its good piezoelectricity compares to other common piezoelectric materials. Table 2.1 lists some common piezoelectric materials for designing SAW devices and their piezoelectric properties. The piezoelectric coupling constant, K^2, describes the efficiency of conversion between electric energy and acoustic energy in piezoelectric materials. K^2 of Y-cut $LiNbO_3$ is the highest among other materials in table 2.1.

Table 2.1: Piezoelectric properties [15].

Material	Cut	Direction	K^2 (%)
$LiNbO_3$	Y	Z	4.6
Quartz	ST	X	0.11
$LiTaO_3$	77.5° rotated Y	90° to X	1.6
GaAs	100	110	0.07

2.4 Design of Focused Interdigital Transducer

To focus the SAWs to the focal point on Y-cut $LiNbO_3$ wafer, the anisotropic effect has to be took in account. The anisotropic effect makes the actual SAWs propagation direction diffracts from the phase velocity angle, which is perpendicular to the IDT fingers. To compute the angle difference that caused by anisotropic effect, the slowness curve is required to be determined accurately [12,13]. The design process

of the FIDT on Y-cut $LiNbO_3$ starts with phase velocity of SAWs in different angles, and inverse phase velocity is the slowness of SAWs. The actual power flow angle can be determined from the slowness curve, so the SAWs propagation direction and velocity, which is the group velocity of SAWs, can be computed. Finally, the polar plot of group velocity is the wave surface of SAWs on Y-cut $LiNbO_3$, and the design of the FIDT is according to this wave surface [18]. The detail of the design process is presented in the next section.

2.4.1 Phase Velocity of Surface Acoustic Wave in Angles

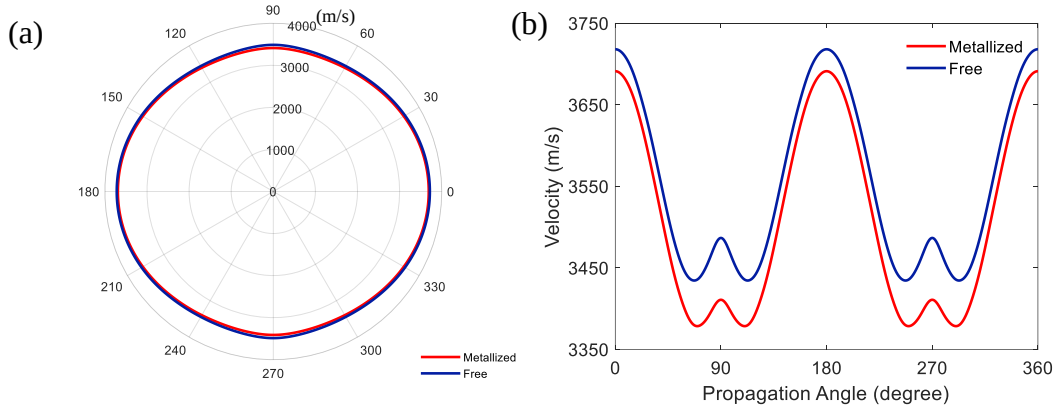

Figure 2.7 (a) Phase velocity plot in polar form. (b) Phase velocity plot in XY coordinate.

First, the phase velocity of the SAW is changing by the angle of propagation on the wafer, figure 2.7 shows the phase velocity of SAW in $LiNbO_3$ [19], here 0 degree is the X axis of the Y-cut $LiNbO_3$ wafer, 90 degree is the Z axis of the wafer. In figure 2.7, we can see the phase velocity of SAW is dependent on the angle of propagation. The phase velocity of SAW in $LiNbO_3$ also depends on the resistivity of the film deposited on top of the piezoelectric material. Figure 2.7 shows two data traces when

the resistivity is zero (Metallized, red trace) and when the resistivity is infinite (Free, blue trace).

2.4.2 Power Flow Angle

In an ideal situation, if the SAW IDTs are infinite along the direction of wave propagation, the SAWs would propagate along the perpendicular direction of the IDTs, which is also the direction of the phase velocity. To design FIDTs, we considered that the curve contains finite number of IDT fingers. As SAWs propagate out of the IDT fingers, the power of the SAWs would propagate into an angle ψ off the perpendicular direction of the IDTs as demonstrated in figure 2.8 below. The angle ψ is called the power flow angle. It is also the direction of group velocity.

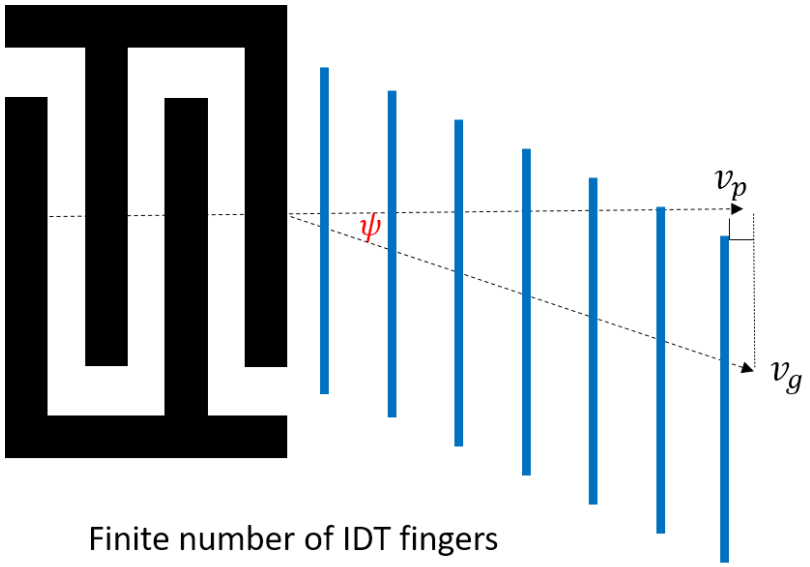

Figure 2.8 Illustration of the angle shift from phase velocity. v_p represents phase velocity, and v_g represents the group velocity.

In figure 2.8, phase velocity is the projection of group velocity with an angle ψ, so it is simply calculated by the following (2.7):

$$v_g = \frac{v_p}{\cos(\psi)} \tag{2.7}$$

where, the v_g is the group velocity, v_p is the phase velocity, ψ is the power flow angle.

The IDT fingers on different angles would have different power flow angle. In designing FIDT on crystalline materials, power flow angle and group velocity are significant parameters that would cause SAWs to be out of focus. In Figure 2.9, six IDT segments represent finite number of IDT fingers in different angle of SAW propagation for demonstration the unfocused SAWs.

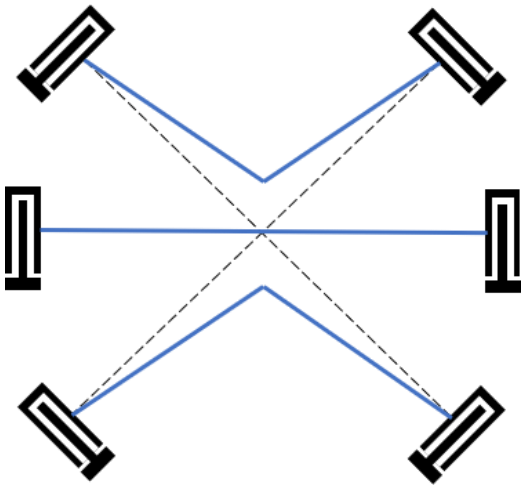

Figure 2.9 Illustration of power flow of SAW diffraction from center. Six IDT segments as demonstrated in the figure represent different angles and distances from the focal point of FIDTs. The dashed line represents the direction of phase velocity, and the blue line represents the direction of group velocity.

Figure 2.9 shows an illustration of how the power of SAW propagates in crystalline materials. The dash lines are the alignments according to the phase velocity in angles, the blue lines are the SAW group velocity direction after the power propagates out the IDT segments. To focus the SAW in this type of structure, we would need to reshape it, and consider that every segment has both correct angle and in equal

phase. In other words, the design should follow the group velocity, instead of phase velocity.

2.4.3 Group Velocity

Group velocity calculation involves calculating the power flow angle and the projecting value of the phase velocity. The experiment of imaging wave surface of SAW on crystalline structure has been done for characterizing the SAW propagation [20]. In order to figure out the shape of FIDTs, we use the inverse concept of the wave surface. When the SAW travels out from a point of source, the source point would create a ripple which is the physical shape of the acoustic wave. The physical shape of the acoustic wave ripple is called wave surface. For a simple example, throwing a rock into a pond will generate a perfect circular ripple moving outward from the source point. But in the case of anisotropic material, due to the different velocities in different angles, shape of the ripple would not be a perfect circle.

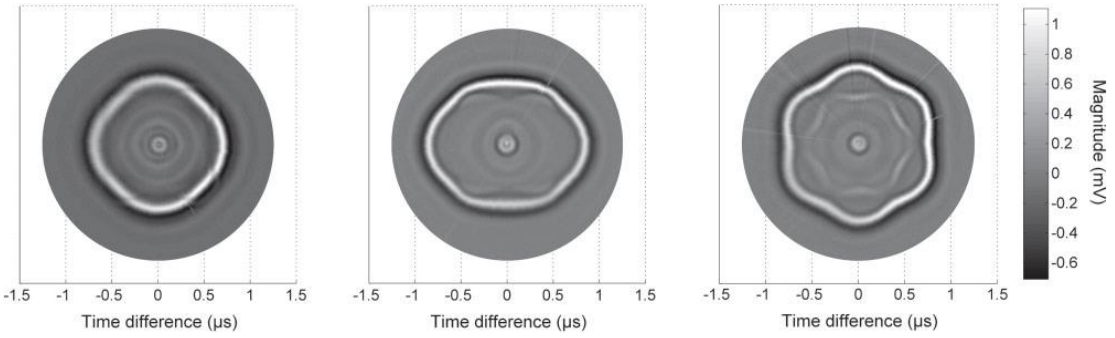

Figure 2.10 Wave surface from a point source in crystalline material. Left picture: Silicon 100, middle picture: Silicon 110, right picture: Silicon 111 (Copyright (2017) The Japan Society of Applied Physics) [20].

In Figure 2.10 shows that the wave surface depends on the crystal structure of the anisotropic material. The experiment imaged the wave surface of [100], [110], and

[111] silicon crystals by using an ultrasonic transducer as the point of source to the silicon crystals. In Park's research [20], they have done the experiment of the wave surface detection, and this result is important for us to design the shape of our FIDT. The following paragraph introduces a key factor for calculating the power flow angle and its connection to wave surface. This key factor is the slowness curve.

A. Slowness Curve

Slowness curve, or slowness surface, is defined as the inverse of phase velocity.

$$s(\theta) = \frac{1}{v_p(\theta)} \tag{2.8}$$

where θ is the direction of phase velocity, $s(\theta)$ is slowness in function of θ. Since the concept of velocity is the distance of the propagation of a wave in a unit of time, so the idea of slowness is the time spent of wave propagation in a unit of distance. In this case, velocity is for calculating the phase equality, because it cares about the time factor. However, the diffraction effect that we mentioned previously, the slowness curve shows the angle of the wave propagation better, because the direction of group velocity is normal to the tangent of the slowness curve. Figure 2.11 illustrates the relationship between slowness curve in function of angle and the power flow angle.

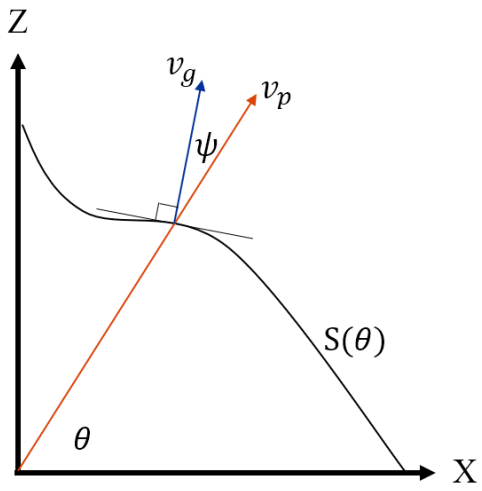

Figure 2.11 Relationship between phase velocity (red), group velocity (blue), and slowness curve ($S(\theta)$).

Thus, the calculation of the power flow angle (ψ) from the slowness curve in the function of θ can be obtained from the flowing equation,

$$\psi = \arctan\left(\frac{ds(\theta)}{d\theta}\right) + 90° - \theta \tag{2.9}$$

Therefore, we have achieved all the components for calculating the group velocity from phase velocity as the function of angle θ.

B. Group Velocity in Lithium Niobate

In our case, Y-cut $LiNbO_3$ wafer was presented as an example of crystalline material. First, the phase velocity data from figure 2.7 [19] was converted into the slowness curve by using (2.8), the inverse of phase velocity. The following figures show the results of slowness curve in two situations, free (resistivity is infinite) and metallized (resistivity is zero).

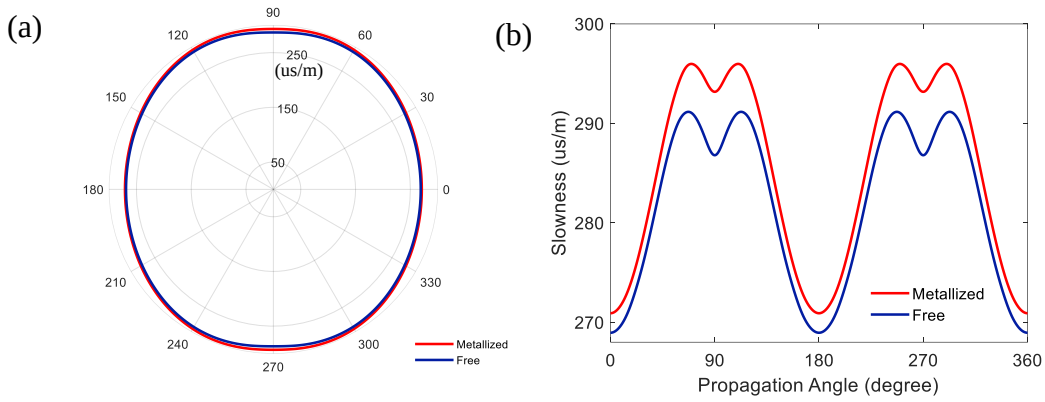

Figure 2.12 (a) Slowness curve of $LiNbO_3$ in polar form. (b) Slowness curve of $LiNbO_3$ in XY coordinate.

In figure 2.12, the two situations are related to the phase velocity plot, in the previous discussion, the phase velocity when the resistivity is zero (metallized situation) is slower than the resistivity is infinite (free). Figure 2.12 shows that the trends of the slowness curves are opposite to the phase velocity, because it is the inverse of the phase velocity. Therefore, the group velocity can be calculated by extracting the power flow angle from the slowness curves and inserting the power flow angle results back into (2.7). The results of group velocity are in the figures below:

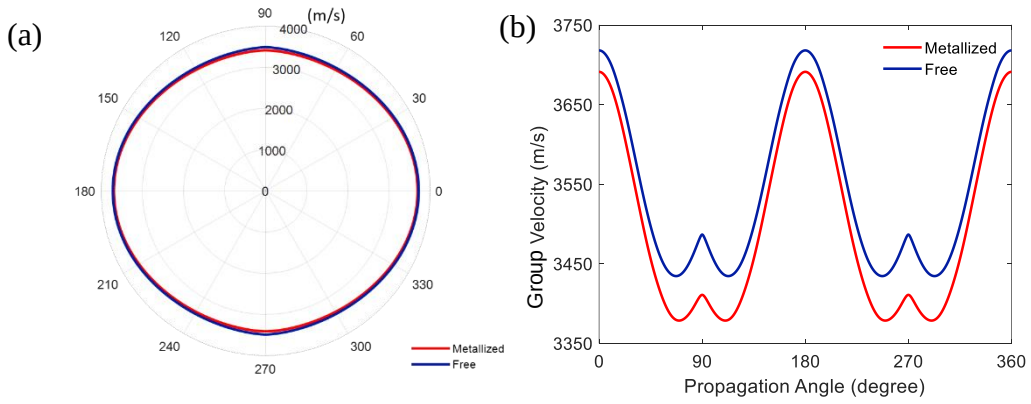

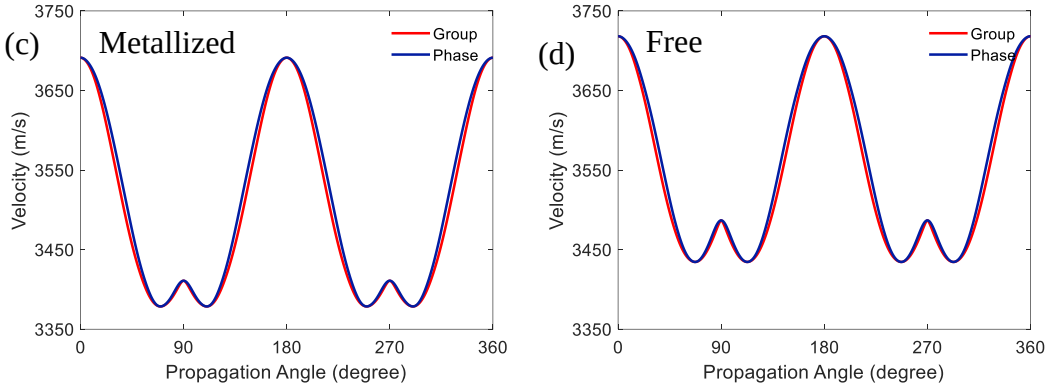

Figure. 2.13 The group velocity results determined by the slowness, power flow angle, and phase velocity that was mentioned in previous sections. (a) Group velocity in polar plot. (b) Group velocity in XY coordinate. (c) Comparison of the phase velocity and group velocity of the metallized situation. (d) Comparison of the phase velocity and group velocity of the free situation.

In figure 2.13, illustrated the results of group velocity calculation in both situations in the function of propagation angle. According to the plots of figure 2.13 (c) and (d), there is no diffraction when the propagation angle is aligning with the Z-axis and X-axis of the wafer, so the group velocity and phase velocity are the same at 0, 90, 270, and 360 degree. Additionally, in figure 2.13 (c) and (d), the group velocity of both metallized and free situations is slower than the phase velocity.

In summary, the polar plot of the group velocity in figure 2.13 (a) is the wave surface of SAW on Y-cut $LiNbO_3$. In the next chapter, the wave surface is going to be used for designing the FIDTs on Y-cut $LiNbO_3$.

Chapter 3 Magnetodynamics and Magneto-Elastic Effects

3.1 Device Layout Design

The layout design process of the FIDTs on crystalline material includes determining the spacing and width of IDT fingers according to the power flow angle and group velocity of the SAW. First, the layout of the FIDTs follows the shape of the wave surface mentioned in the previous chapter. The design of the FIDTs uses the reverse concept of the wave surface, we place the IDT fingers according to the wave surface. Therefore, a SAW generated from IDTs would be focused at the center of the wave surface.

Secondly, the wave surface and the group velocity plot are the same shape. To obtain the wave surface of Y-cut $LiNbO_3$ wafer, we have determined the group velocity into polar form in figure 2.13 (a) in the previous chapter. The design of FIDTs is targeted to excite SAWs at 1.5 GHz. The wavelength of 1.5 GHz SAW is the minimum wavelength, that can be detected by our heterodyne interferometer. However, due to fabrication limits in our cleanroom facility, the minimum size of circuit that we can make is 0.8 μm. It is impossible to build a device with 1.5 GHz fundamental frequency, because the spacing of the IDT fingers with 1.5 GHz fundamental frequency is less than 0.6 μm. Therefore, we fabricated a FIDT device with 500 MHz fundamental frequency, and generated the SAWs on the third harmonic frequency, which is 1.5 GHz. Based on the fundamental frequency, 500 MHz, we used the equal spacing and width for the FIDT fingers and calculated the spacing of each angle from the group velocity results.

Finally, we fabricated a FIDT device that has Aluminum (Al) for the conductor on Y-cut $LiNbO_3$ wafer. The Al was deposited by RF sputtering to 100 nm, and lift-off of Al from the unwanted area. As a result, figure 3.1 is an image of the FIDTs device (see Appendix A for more designing details).

Table 3.1 (a): IDT fingers in metallized situation

	Spacing (μm)	Wavelength Fundamental (μm)	Wavelength 3rd Harmonic (μm)	Group Velocity (m/s)
90°	1.706	6.822	2.274	3411
60°	1.696	6.784	2.261	3392
30°	1.778	7.112	2.371	3556
0°	1.846	7.382	2.461	3691

Table 3.1 (b): IDT fingers in free situation

	Spacing (μm)	Wavelength Fundamental (μm)	Wavelength 3rd Harmonic (μm)	Group Velocity (m/s)
90°	1.744	6.974	2.325	3487
60°	1.721	6.882	2.294	3441
30°	1.797	7.186	2.395	3593
0°	1.859	7.436	2.479	3718

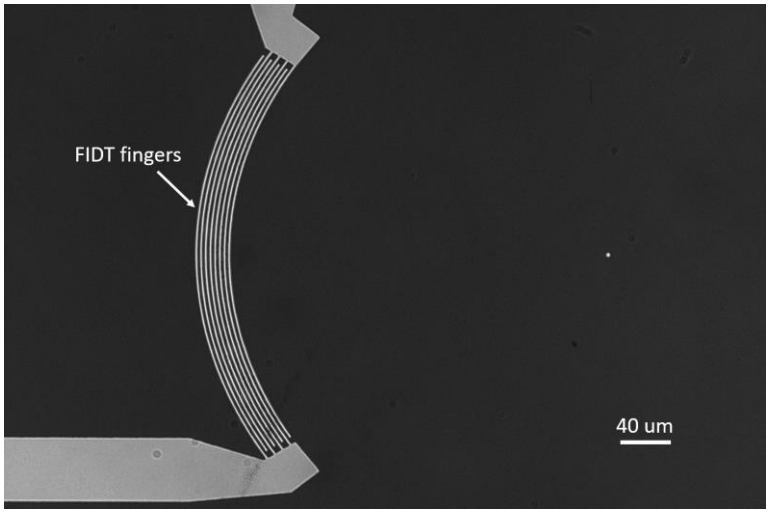

Figure 3.1 Image of FIDT fingers taken at 20x magnification.

3.2 Field-Free Precessional Magnetization Switching

In this section, we will present the process of field-free magnetization switching of a ferromagnetic thin film by applying surface acoustic waves. Traditionally, the way to switch or reverse the direction of the magnetization is to apply an external magnetic field opposite to the direction of the initial magnetization. The external field has to be strong enough to overcome the coercivity and reverse the magnetization [21]. However, to accomplish the field-free magnetization switching, we introduce precessional switching. Instead of applying a field opposite to the initial magnetization, the precessional switching applies an AC field at an angle that is not parallel to the direction of initial magnetization [22]. The reason for applying an angle is to control the magnetization precessional motion by using the associated torque that is created by the difference of the angle between the external field and initial magnetization.

3.3 Precessional Switching by Surface Acoustic Waves

A regular precessional switching process includes two steps. First, the magnetization starts precessing by the effect of the external field until it almost flips to the other direction. The second step is removing the external field, therefore, the magnetization starts damping out to the direction of the nearby equilibrium point [22]. However, this regular precessional switching does not satisfy the goal of this research, which is the field-free switching. For field-free switching, we introduce the precessional switching by surface acoustic waves. The method of using SAWs for precessional switching is a relatively new concept starting in the last decade [3,4].

Some research has been done to prove that SAWs can reverse the magnetization of the sample under certain conditions, such as controlled temperature, and short distance from SAW IDT [3,4]. However, none of them achieve field-free switching without controlling the precondition of the sample, such as the switching must be operated under the curie temperature. Therefore, we use the FIDT to achieve this goal of field free switching.

3.4 Villari Effect and Anisotropic Field

The SAWs can provide the effective field that changes the direction of magnetization domain by the Villari effect. The Villari effect describes how the stresses applied to the sample can generate the effective field by the following [23]:

$$E_\sigma = \frac{3}{2}\lambda_s \sigma_s sin^2(\theta_s)\ [\mathrm{J/m^3}] \tag{3.1}$$

where the E_σ is the free energy density, λ_s is magnetostriction coefficient, σ_s is the stress applied to the sample, and θ_s is the angle between the direction of stress and magnetization. This equation is usually written as

$$E_\sigma = Ksin^2(\theta_s)\ [\mathrm{J/m^3}] \tag{3.2}$$

where K is defined as the uniaxial anisotropy constant with $K = \frac{3}{2}\lambda_s \sigma_s$ an important factor to determine the effective inverse magnetostrictive field generated by the stress. The effective inverse magnetostrictive field has the form of an uniaxial anisotropy, and it can be obtained from [24]:

$$\boldsymbol{B_m} = \frac{2}{M_s}[(K_1 + 2K_2)(\boldsymbol{m}\cdot\boldsymbol{e}) - K_2(\boldsymbol{m}\cdot\boldsymbol{e})^3]\boldsymbol{e} \tag{3.3}$$

where $\boldsymbol{B_m}$ is the inverse magnetostrictive field, K_1 and K_2 are the first order and second order of the anisotropic constant, $\boldsymbol{e}$ is the easy axis direction, and $\boldsymbol{m}$ is the unit vector of the magnetic moment ($\boldsymbol{M}$) which is defined by $\boldsymbol{M}/M_s$. In our simulation in the next chapter, we will ignore the second order of the anisotropic constant (K_2) and only take the first order of the anisotropic constant (K_1) into account for the simulation. After the anisotropic field is obtained, we introduce the Landau-Lifshitz equation for describing the dynamical movement of magnetization.

3.5 Magnetodynamics

The Landau–Lifshitz equation is commonly used for describing the response of magnetization to a time varying magnetic field, which we use the Villari effect to achieve. The Landau–Lifshitz equation is as the follows [25]:

$$\frac{d\boldsymbol{M}}{dt} = -\gamma \boldsymbol{M} \times \boldsymbol{H_{eff}} - \lambda \boldsymbol{M} \times (\boldsymbol{M} \times \boldsymbol{H_{eff}}) \tag{3.4}$$

where γ is gyromagnetic ratio, which is a constant $1.76 \times 10^{11}[rad/sT]$. λ is a damping parameter determined by γ, M_s, and α, the damping factor. The relationship is shown below [23]:

$$\lambda = \alpha \frac{\gamma}{M_s} \tag{3.5}$$

The most important parameter in (3.4) is $\boldsymbol{H_{eff}}$, effective field. The effective field contains three terms:

$$\boldsymbol{H_{eff}} = \boldsymbol{H_{bias}} + \boldsymbol{H_d} + \boldsymbol{H_m} \tag{3.6}$$

where $\boldsymbol{H_{bias}}$ is the external bias field, $\boldsymbol{H_d}$ is the demagnetization field, and $\boldsymbol{H_m}$ is the magnetoelastic field. $\boldsymbol{H_d}$ depends on the demagnetization factor (N) is a tensor according to the shape of the ferromagnetic sample, as $\boldsymbol{H_d} = -N\boldsymbol{M}$. $\boldsymbol{H_m}$ can be

determined by the inverse magnetostrictive field ($\boldsymbol{B_m}$) that we introduced in the last section, as $\boldsymbol{H_m} = \boldsymbol{B_m}/\mu_0$. As a result, we can plug $\boldsymbol{H_{eff}}$ back into (3.4) and obtain the magnetization dynamically in time. In the next chapter, we demonstrate simulation results according to the dynamic equation of magnetization from this section.

Chapter 4 Experiment and Simulation Results

4.1 Surface Acoustic Wave Interferometer Measurement

For experimental measurements, we target the third harmonic of the FIDT, which is 1.5 GHz. Although it was found the FIDT responds to higher harmonics (e.g. 5^{th}, 7^{th} at 2.5 GHz and 3.5 GHz), the associated wavelengths are too small to observe with our heterodyne interferometer setup. The frequency response is shown in the figures below in:

(a)

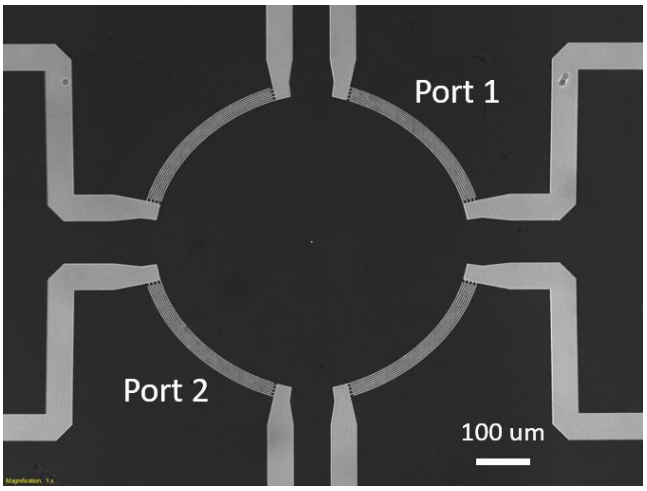

(b)

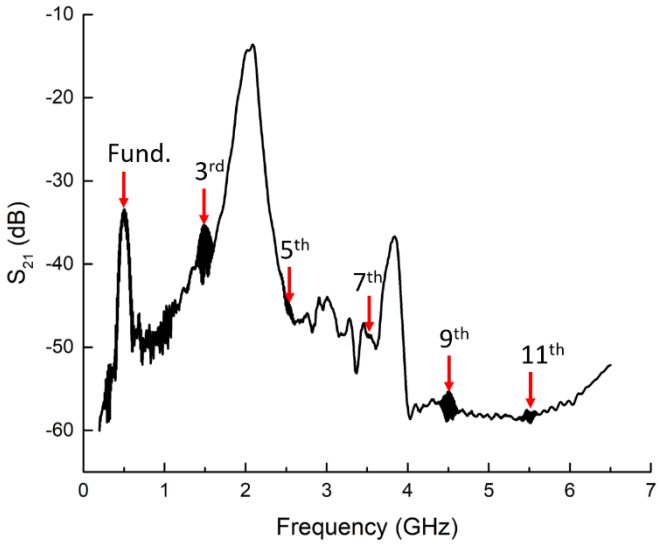

Figure 4.1 (a) The image of the device for measuring frequency response purpose. (b) S_{21} of the device in figure 4.1 (a).

In figure 4.1 (a), four channels of FIDT are included in the device only for measuring the frequency response purpose, because the opposite FIDT fingers can be the receiver of SAWs. The FIDT fingers, that labeled Port 1, are connected to port 1 of VNA, and the FIDT fingers, that labeled Port 2, are connected to port 2 of the VNA. The frequency response of fundamental frequency (500 MHz), 3rd harmonic (1.5 GHz), and 9th harmonic (4.5 GHz) are clear shown in figure 4.1 (b), but the 5th harmonic (2.5 GHz), 7th harmonic (3.5 GHz), and 11th harmonic (5.5 GHz) are not obvious in figure 4.1 (b).

For the interferometer measurement, we have used a device with only one channel of FIDT. The purpose of the experimentations described is to determine the focus spot size for the FIDT channel, as well as the SAW wavelength. Although the proposed design for magnetization switching (which will be described for the simulation in section 4.2 of this chapter) has two FIDT channels, for the experiment, the opposite channel is not fabricated on our device. This is because the opposite channel can reflect the SAW generated from the first channel, and hence the interference between these two waves may create a standing wave. To measure the focus spot precisely, we need to eliminate the standing wave (as the standing wave will create local nodes and anti-nodes).

4.2 Experimental Setup

Figure 4.2 is the photo of the actual interferometer setup on an anti-vibration table. The network analyzer used is a Keysight E5071C. A RF signal generator (Agilent N5183A) and a spectrum analyzer (Tektronix RSA3303B) are used for the

interferometer, but they are not included in figure 4.2. Figure 4.3 is a photo of the customized probe station and the $LiNbO_3$ substrate with FIDTs device under testing.

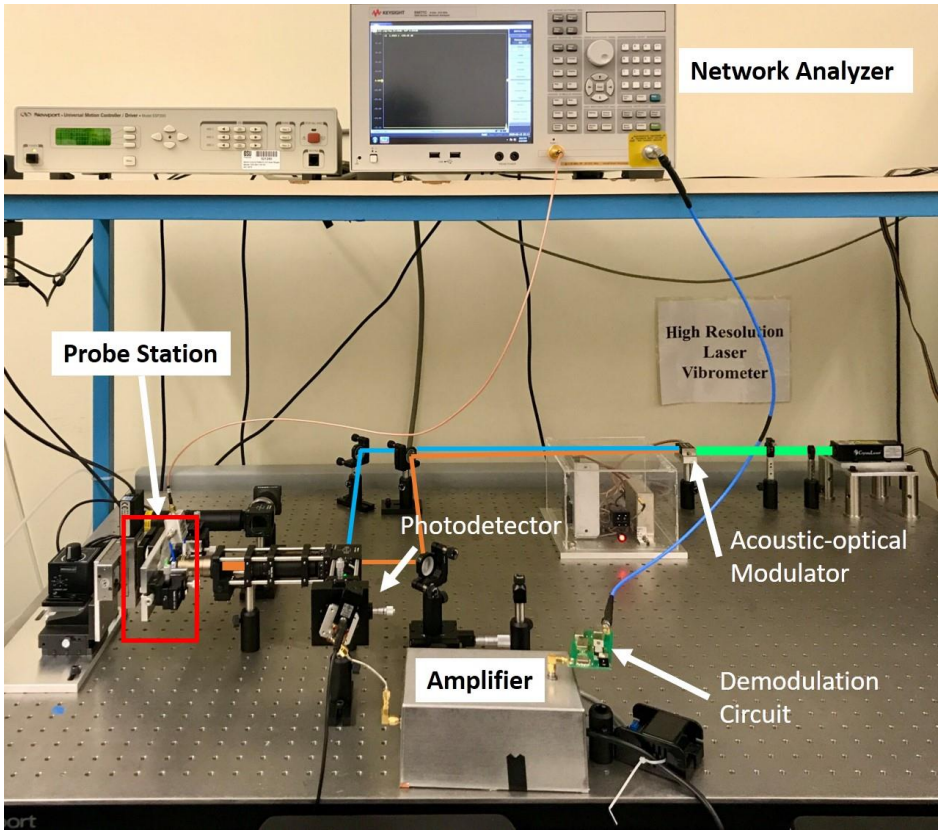

Figure 4.2 The interferometer setup.

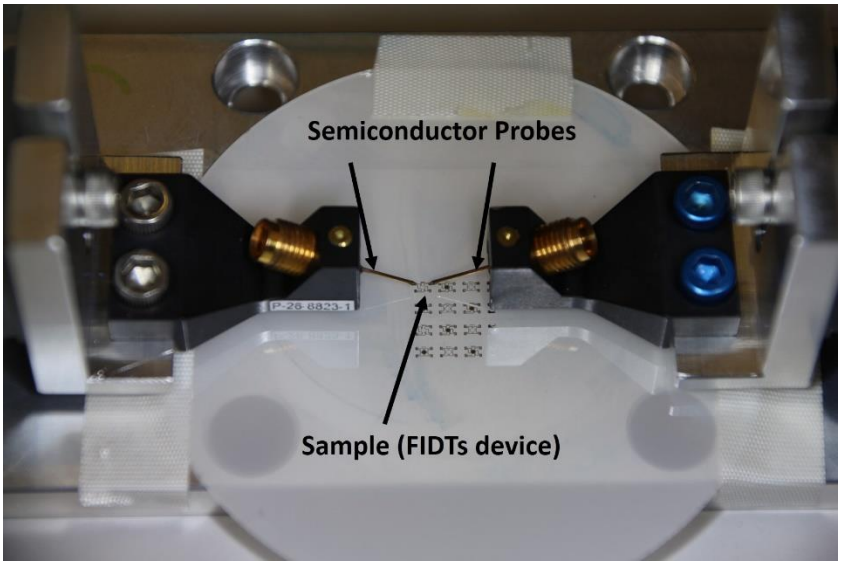

Figure 4.3 Probe station setup for interferometer measurement.

4.3 Experimental Results of Interferometer Measurement

For the first experiment to determine the wavelength of the SAW, the signal input is given from port 1 of the VNA, driven at 1.5 GHz with the maximum output power of VNA, 10 dBm. This signal excites the FIDT to generate SAW that can focus to a certain point. Figure 4.4 below illustrates the SAW generation from FIDT. The results are shown in figure 4.5.

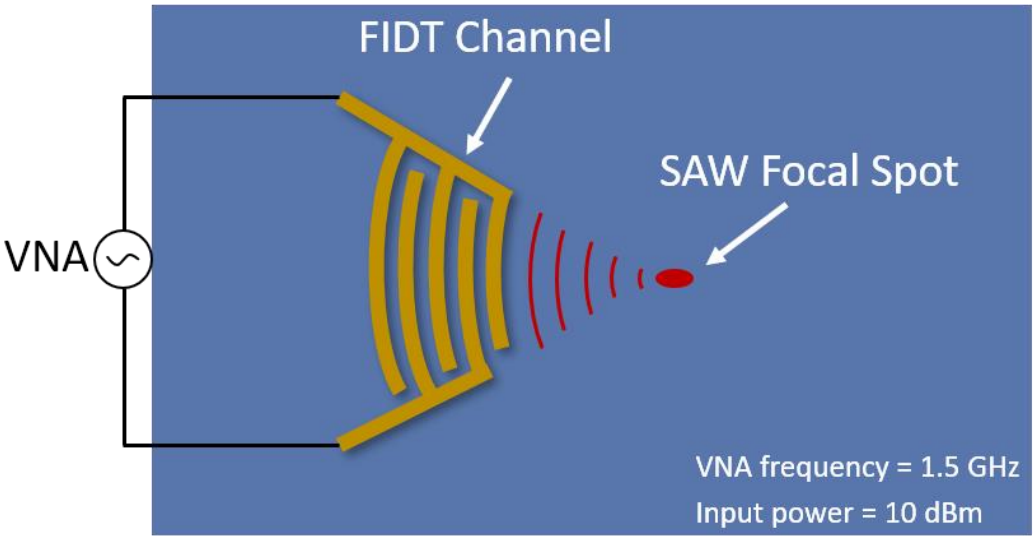

Figure 4.4. Focused IDT fingers and illustration of the SAW focusing.

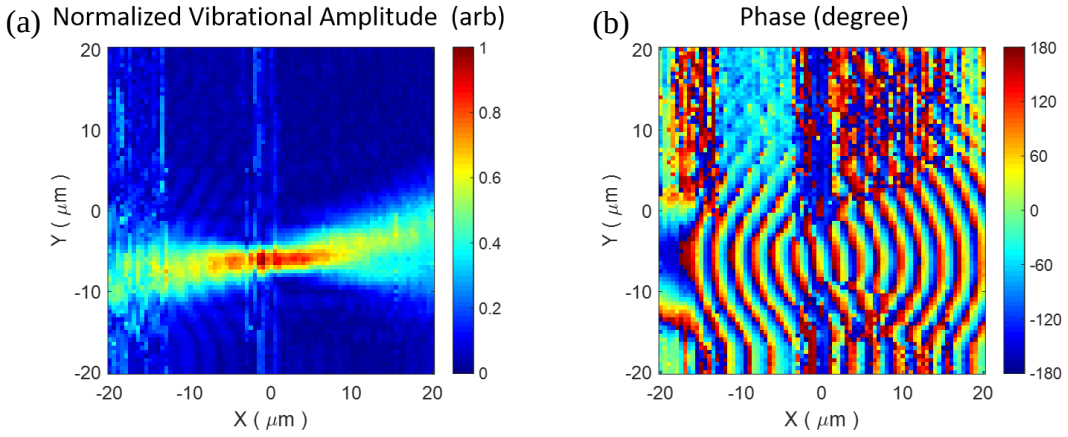

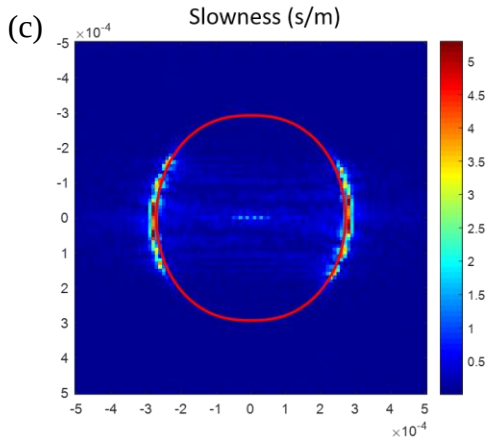

Figure 4.5 Interferometer measurement results measured in an area of 40 μm by 40 μm with 0.5 μm step size. (a) The normalized vibrational amplitude of SAWs. (b) The phase of SAWs. (c) The result of 2D spatial Fourier transform of magnitude and phase measurement. Red curve is the slowness curve that we determined from figure 2.12 (a).

Due to the pure traveling wave of the SAWs, we should not see any wave front in the vibrational amplitude measurement. However, the wave fronts are still visible in figure 4.5 (a), because of the RF interference received by the demodulator circuit. The phase measurement in figure 4.5 (b) shows periodic behavior, and we can use this periodicity to measure the wavelength of the SAWs. The wavelength of the third harmonic is measured as 2.5 μm (average of seven periods) from figure 4.5 (b), which is in good agreement to the theoretical value of 2.47 μm (calculated from table 3.2). Moreover, figure 4.5 (c) shows the slowness curve result, which is determined by the spatial 2D Fourier transform of figure 4.5 (a) and figure 4.5 (b). The shape matches to the slowness curve for the Y-cut $LiNbO_3$ shown in figure 2.12 (a).

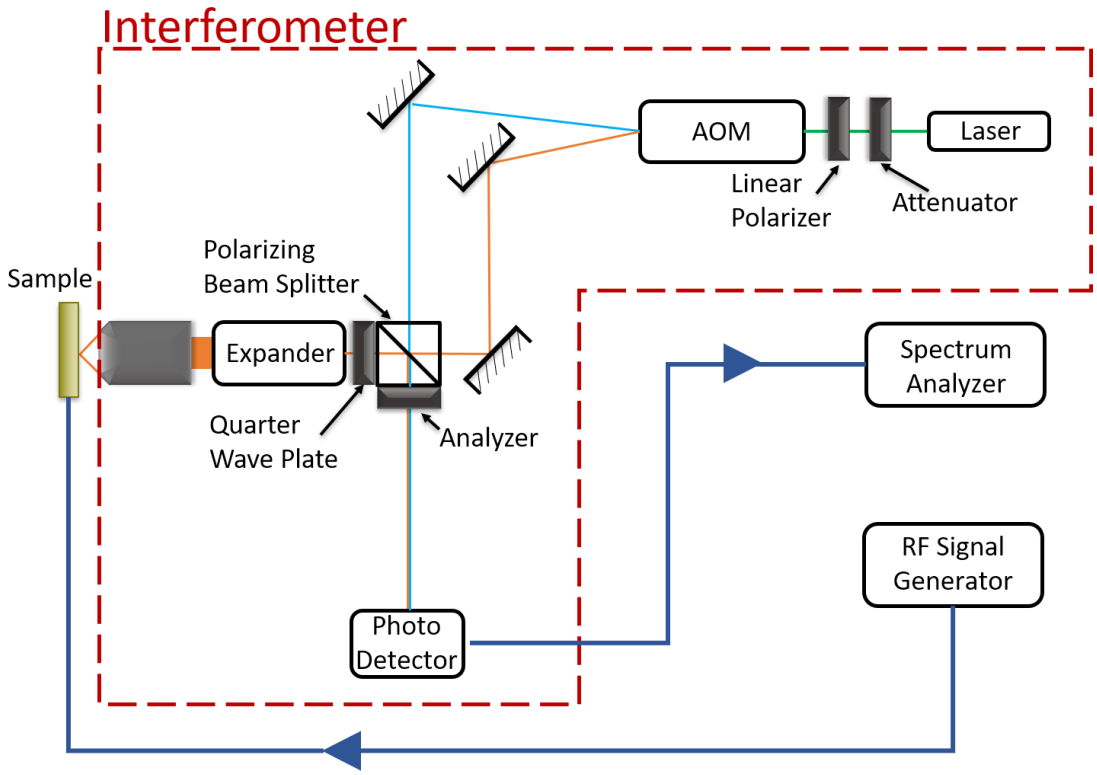

Figure 4.6 Interferometer setup of the measurement with RF signal generator and spectrum analyzer.

For the second experiment to measure the area of the focus spot of the SAWs, a RF signal generator is used to generate input signals for the FIDTs, and a spectrum analyzer is used to detect the receiving signal from photodetector. The layout of the equipment for this experiment is shown in figure 4.6. Using this setup, the spectrum analyzer can directly analyze the signal from the photodetector without demodulation, so that we can eliminate the interference from the demodulator circuit and determine the vibrational amplitude of the travelling SAWs. Therefore, the focal spot size can be measured accurately without being affected by unknown signal. The results are shown in figure 4.6.

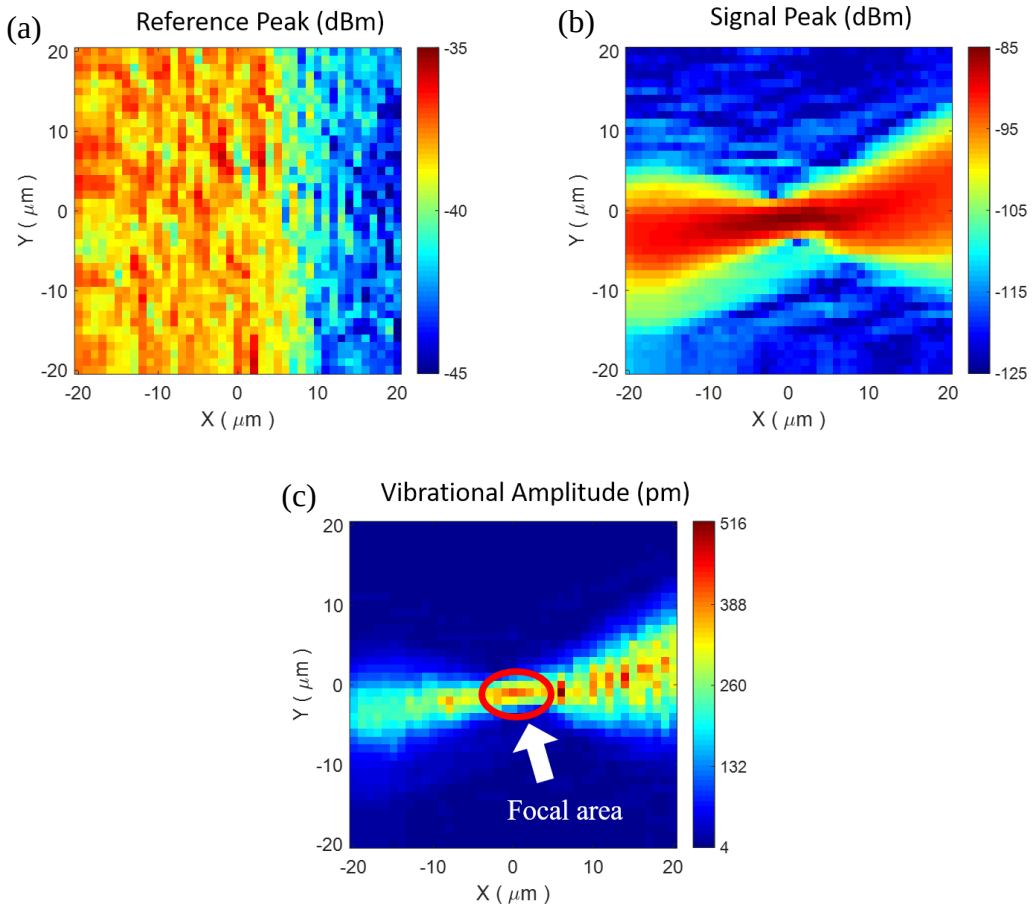

Figure 4.7 Interferometer measurements with signal generator and spectrum analyzer setup. The scan area is 40 μm by 40 μm with 1 μm step size. (a) Reference peak power in dBm at 200 MHz. (b) Signal peak power in dBm at 1.7 GHz (f_{saw} + $f_{reference}$). (c) Amplitude of the acoustic vibration.

The AOM heats up over time as we scan the device, and as a result, the reference power decreases significantly. This is evident in the right-hand part of the reference power plot shown in figure 4.7 (a). Therefore, some data in the right portion of figure 4.7 (c) show higher vibrational amplitude compared to the focal point in the center. However, most of the data from this measurement are still trustworthy. Figure 4.7 (c) is the result that is determined from the reference peak power in figure 4.7 (a) and signal peak power in figure 4.7 (b) by using (2.6) in chapter 2. The acoustic vibrational amplitude of the

focal point is determined to be 407 pm. Note that the highest vibration amplitude, 516 pm, is not at the focal point.

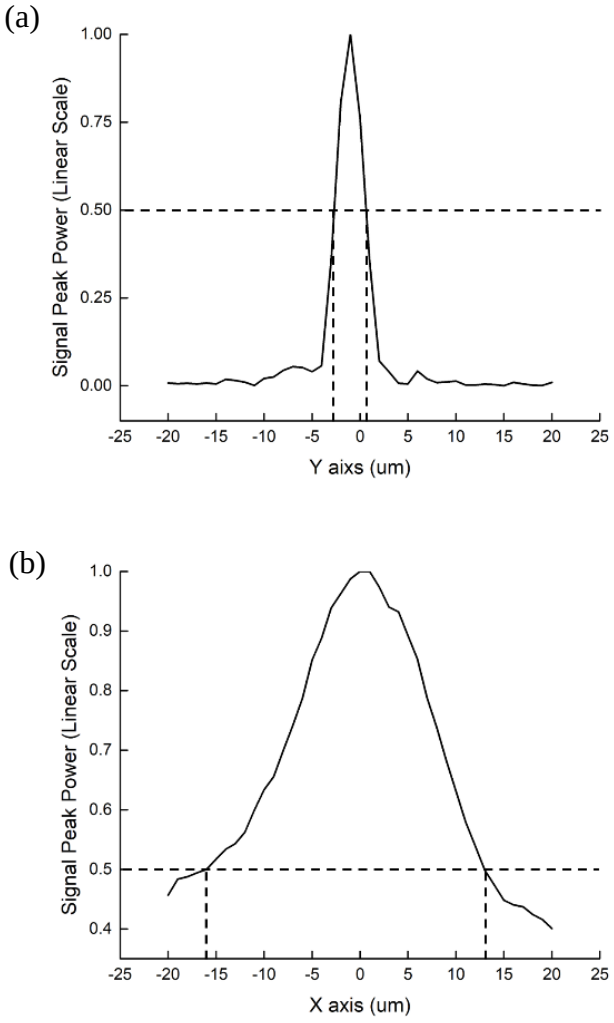

Figure 4.8 Cross-cut plots of figure 4.7 (b) on both x-axis and y-axis. These figures are normalized to the maximum vibrational amplitude and converted into linear scale.

We can determine the focal spot size and the SAW focal area from figure 4.8, where we show the normalized signal peak power along the x and y-axis. Figure 4.8 (a) shows the cross-section of y-axis of the signal peak power from figure 4.7 (b), the focal spot size is determined as ~5 μm in the y-axis (according to the half-power dashed line). Similarly, the focal spot size in the x-axis is observed as ~30 μm from figure 4.8 (b).

In summary, the acoustic vibrational amplitude, wavelength, and focal area of the SAW were determined. These are fundamental parameters required to develop a precessional switching simulation. The next section introduces the method of field-free precessional switching and demonstrates the simulation results from the MATLAB® calculation by using all the FIDT's properties that we have measured in this section.

4.4 Field-Free Precessional Switching Simulation

The proposed device for the field-free magnetization switching has two orthogonal FIDT channels and a magnetostrictive material at the focal spot. For our simulation, we chose nickel (Ni) as the magnetostrictive material, due to the inability of sputtering other magnetostrictive material. A schematic of the proposed design is shown in figure 4.8.

The process of the field-free precessional switching in this research includes two steps: first, a SAW burst (from Channel 1) is applied at 45° from the initial magnetization direction to generate an acoustic strain. This strain from this SAW burst creates an anisotropic field through Villari effect on the ferromagnetic sample and hence, changes the magnetization direction away from the initial state. Secondly, as soon as the magnetization precesses to the angle furthest away from the initial direction, the first SAW burst will be turned off and another SAW burst (from Channel 2) will be excited at -45^0 from the initial magnetization direction immediately. The purpose of this second SAW burst is to pull the magnetization across the hard axis. As a result, the magnetization will be reversed to the other direction. The following figure 4.9 shows the steps for the process of precessional switching by focused SAWs.

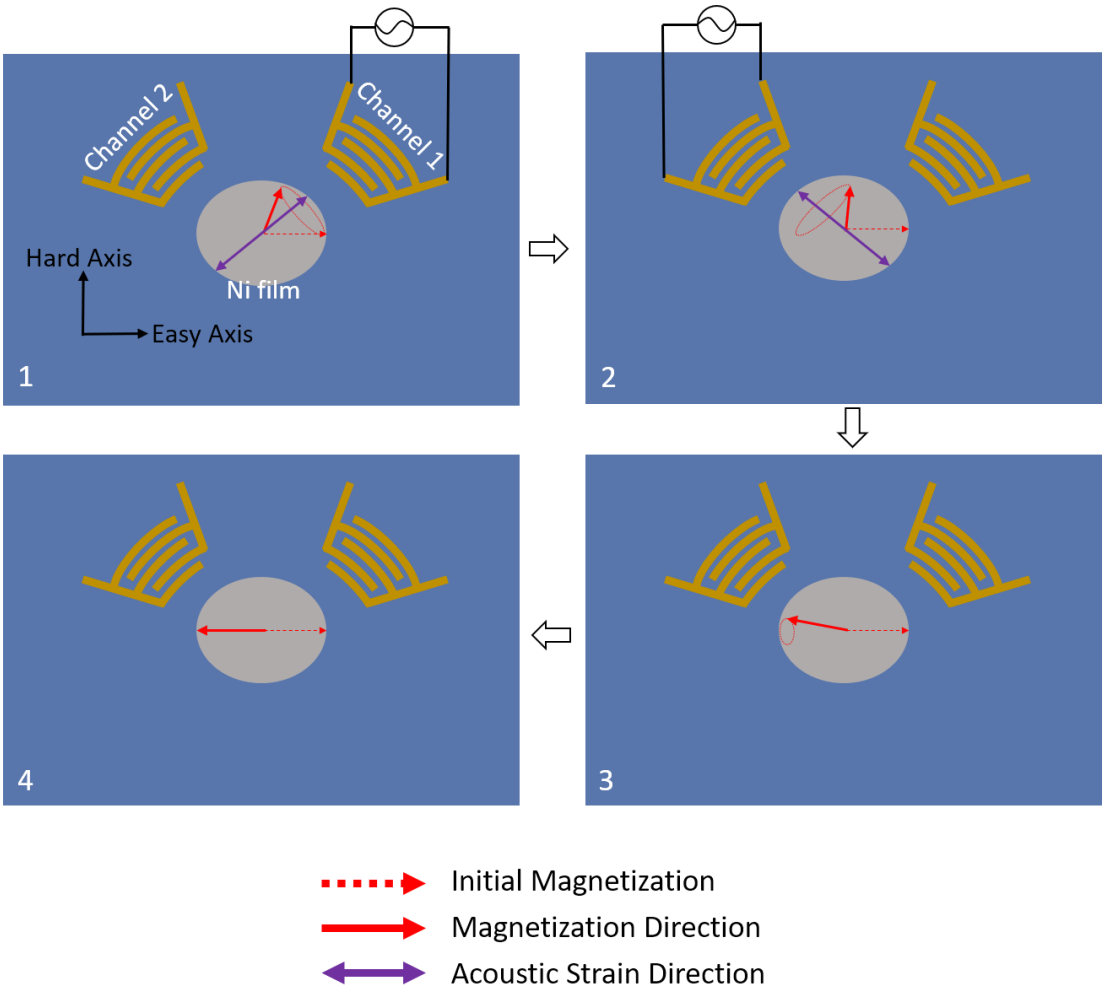

Figure 4.9 The process of precessional magnetization switching operation with two FIDT devices. The red dash arrow represents the initial direction of the magnetization along the easy axis. The red solid arrow shows the dynamic magnetization. The purple double arrow is the direction of the acoustic strain that is generated by the SAW burst.

To simulate this process, we need to know two things: the strain value that can be generated from the SAW burst and secondly, the demagnetization factor of the sample that depends on the shape of the Ni film on the focal spot. The in-plane strain generated by the SAW burst is determined from the acoustic vibrational amplitude in the focal spot (calculated from the interferometry measurement performed in section 4.3, 407 pm for 10 dBm SAW power). This in-plane strain will be converted into stress in the Ni film, according to the following equation.

$$\sigma_s = \varepsilon_s Y sin(\omega_{SAW} t + kx) \quad (4.1)$$

where, Y is the Young's modulus of Ni, ε_s is the in-plane strain for the direction of x-axis of $LiNbO_3$, and σ_s is the stress in the Ni film as we are assuming that in-plane strain for the Ni film will be equal to the strain in the $LiNbO_3$ substrate. Young's modulus, Y for the Ni film is 2.20×10^{11} [J/m^3] [26]. The in-plane strain (ε_s) along the x-axis in the $LiNbO_3$ is calculated by,

$$\varepsilon_s = \frac{u_x}{u_z} Ak \quad (4.2)$$

where, k is the wavenumber of the SAWs, u_x/u_z is the ratio of in-plane and out-plane displacement and is 0.7 [27]. The wavenumber, k is determined as 2.53 [1/μm] from the interferometry experiment. A is the acoustic vibrational amplitude. Therefore, the stress that is applied on the ferromagnetic material is determined. According to (3.2), the uniaxial anisotropy constant (K) can be determined by $K = \frac{3}{2}\lambda_s \sigma_s$ as . Finally, with the value of K, the magnetoelastic field ($\boldsymbol{H_m}$) is also determined.

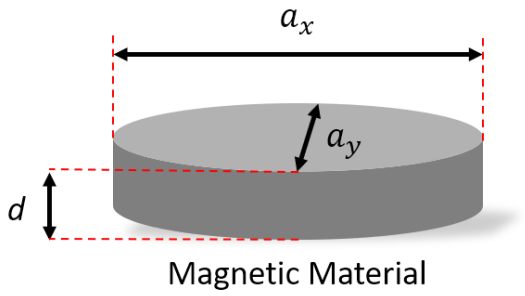

Figure 4.10 Illustration of the dimension of a magnetic material and its relationship with demagnetization factor. a_x and a_y indicate the dimension in x and y direction, respectively. d indicates the thickness.

According to the Landau–Lifshitz equation, to calculate the $\boldsymbol{H_{eff}}$, the demagnetization field ($\boldsymbol{H_d}$) is a required term for $\boldsymbol{H_{eff}}$. The demagnetization field is defined as, $\boldsymbol{H_d} = -N\boldsymbol{M}$, where N is the demagnetization factor, and $\boldsymbol{M}$ is the

magnetization. In order to match the FMR frequency to the frequency of SAWs, we need to specify the values for the demagnetization factors (N_x, N_y *and* N_z) for the three directions, and they are inverse proportional to the dimension of the magnetic material shown in figure 4.10 (N_x:N_y:N_z = 1/a_x: 1/a_y: 1/d). The resonant frequency of the FMR is:

$$\omega_{FMR} = \gamma\mu_0\sqrt{[(N_y - N_x)M_s + H_{bias}][(N_z - N_x)M_s + H_{bias}]} \qquad (4.3)$$

The H_{bias} is zero in this calculation (since our process is field-free), and the sum of N_x, N_y, and N_z is one. For our simulation, we use 100 nm as the thickness of the Ni thin film for determining the demagnetization factor, and N_z is assumed as 0.8 for simplifying the math. Since, $\omega_{SAW} = 1.5 \times 10^9 \times 2\pi\ [rad/s]$, and $M_s = 4.7 \times 10^5\ [A/m]$ [28], the N_x and N_y are determined as 0.094 and 0.106 respectively by (4.3) in order to match ω_{FMR} to ω_{SAW}. The following equation determines the dimensions of Ni thin film for the future implementation [29]:

$$N_x \approx \frac{2d}{\pi a_x},\ N_y \approx \frac{2d}{\pi a_y} \qquad (4.4)$$

where, d is the thickness of the Ni film (100 nm). a_x and a_y are the dimension of the easy axis and hard axis, respectively. a_x is determined as 0.667 μm, and the a_y is determined as 0.601 μm. The values of N_x and N_y are imported into the precessional switching module that we have developed with MATLAB®. The damping parameter for Ni is 0.04 [28]. The FMR of free decaying Ni film in damping parameter = 0.04 condition is shown in figure 4.11:

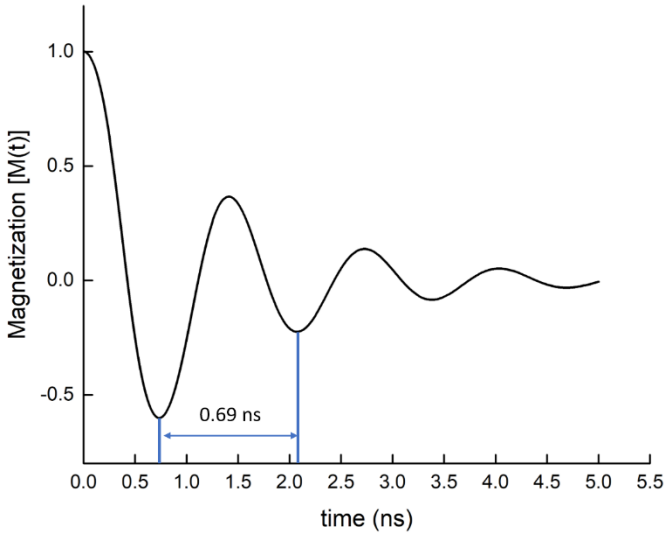

Figure 4.11 FMR simulation of free decaying Ni with the demagnetization factor $(N_x, N_y, N_z) = (0.094, 0.106, 0.8)$.

Figure 4.11 shows the damped oscillatory behavior of the normalized magnetization in-plane. Figure 4.11 demonstrates the magnetization oscillation as a function of time, and the period is determined as 0.69 ns. As a result, the FMR frequency for Ni, with the demagnetization factor (N_x, N_y, N_z) = (0.094, 0.106, 0.8), is 1.45 GHz, so we will use this demagnetization factor in the simulation of precessional switching. In the simulation, a SAW burst from channel 1 (in the [1 1 0] direction) with 1.5 GHz is turned on from 0 ns to 0.1 ns time interval, and another SAW burst from channel 2 (in the $[-1\ 1\ 0]$) with the same frequency is turned on from 0.1 ns to 0.2 ns.

(a)

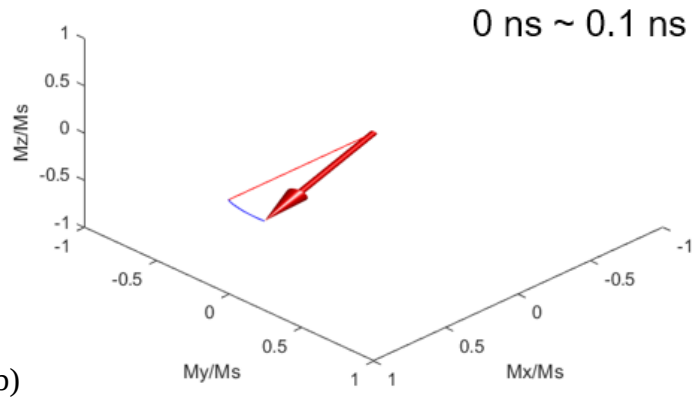

(b)

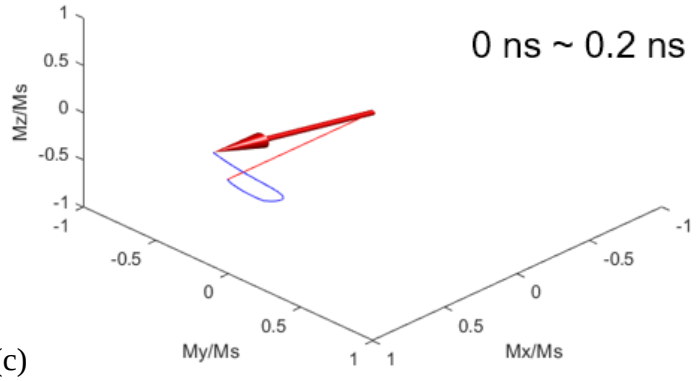

(c)

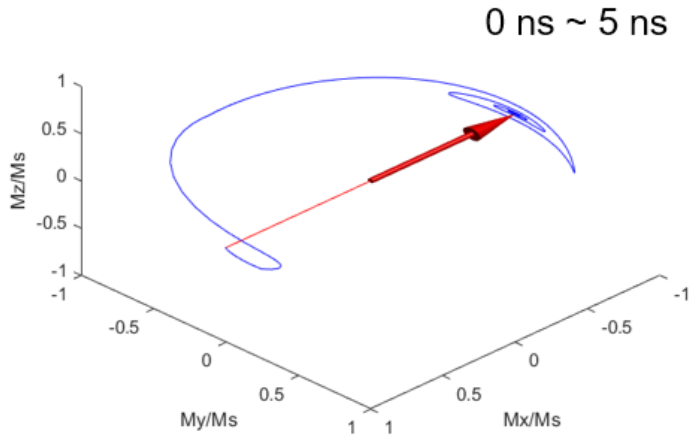

Figure 4.12 Simulation of magnetization switching with 400 pm vibrational amplitude, and 0.1 ns SAW burst duration for both channel 1 and 2. The red arrow represents the magnetization at the end of time period. The blue line is the trace of the arrow tip traveled. The red straight line is the initial magnetization direction [1 0 0]. (a) Time interval: 0 ns~0.1 ns. (b) Time interval: 0 ns~0.2 ns. (c) Time interval: 0 ns~5 ns, whole switching.

(a)

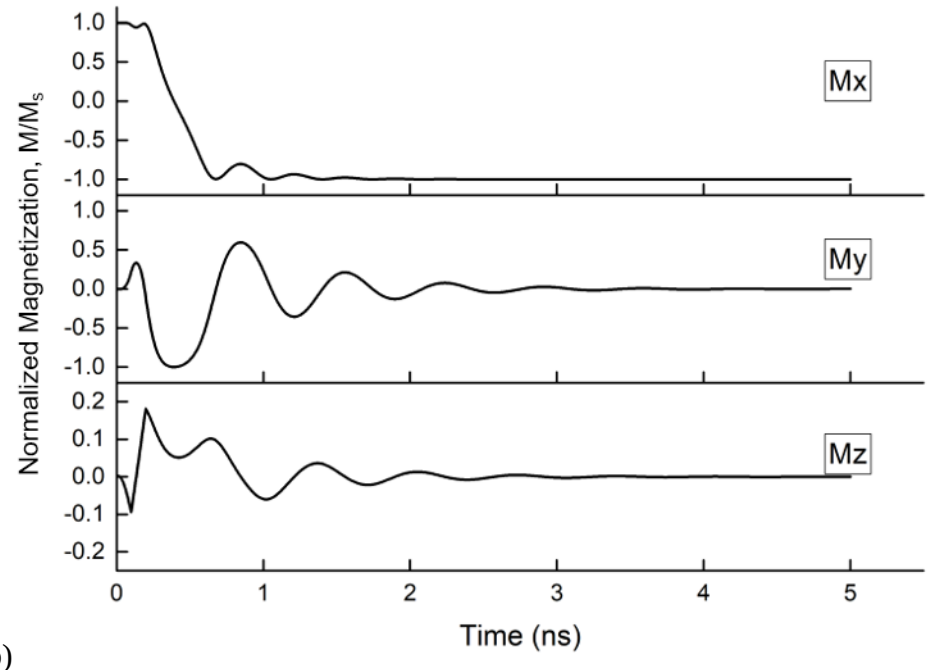

(b)

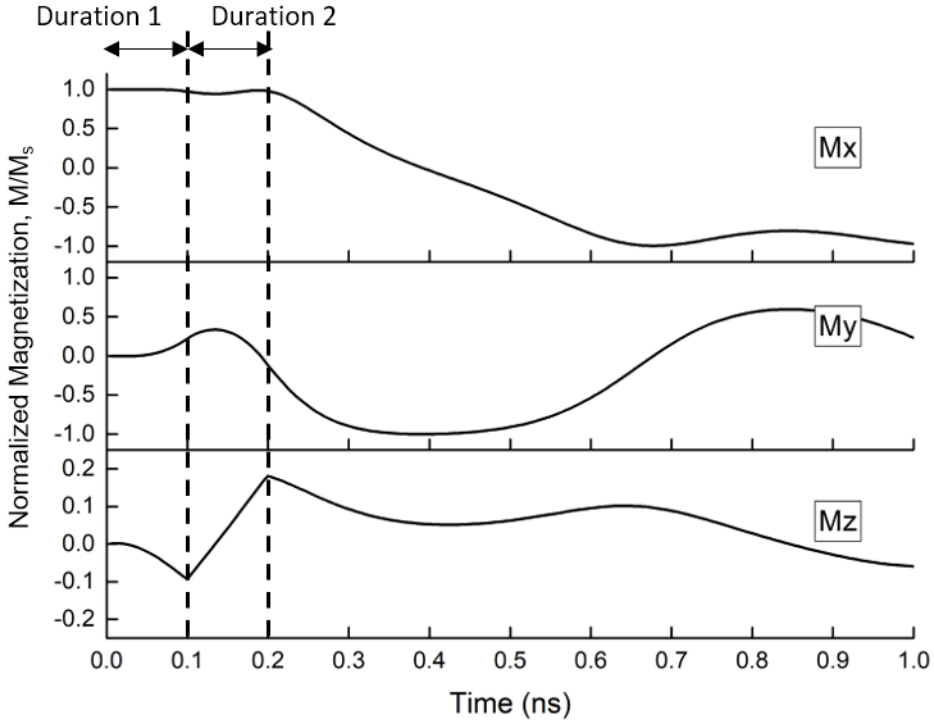

Figure 4.13 Results of magnetization direction in function of time. (a) Whole simulation from 0 ns~5 ns. (b) Simulation from 0 ns~1 ns. From 0 ns to 0.1 ns is the 45-degree SAW burst turned on, 0.1 ns to 0.2 ns is the -45-degree SAW burst turned on.

According to the simulation results in figure 4.12 and figure 4.13, the magnetization can be successfully reversed. In figure 4.13 (b), the effect of acoustic strain on the magnetization is shown. We can see that magnetization in the x-direction, $M_x = 4.7 \times 10^5\ [A/m]$ at time = 0 ns and at time ~ 2 ns, $M_x = -4.7 \times 10^5\ [A/m]$. However, the time period a 1.5 GHz SAW is 2/3 ns. It is impossible for the FIDT to generate a SAW burst with 0.1 ns duration. Therefore, we need to simulate this process with a time duration which is greater than the SAW period. This is illustrated in figure 4.14, where x and y-axis show the number of time periods (cycles) each FIDT is on. The black color means the magnetization reversal is not achieved, the red color indicates the successful reversal of the magnetization, and the gray scale indicates multi-reversal.

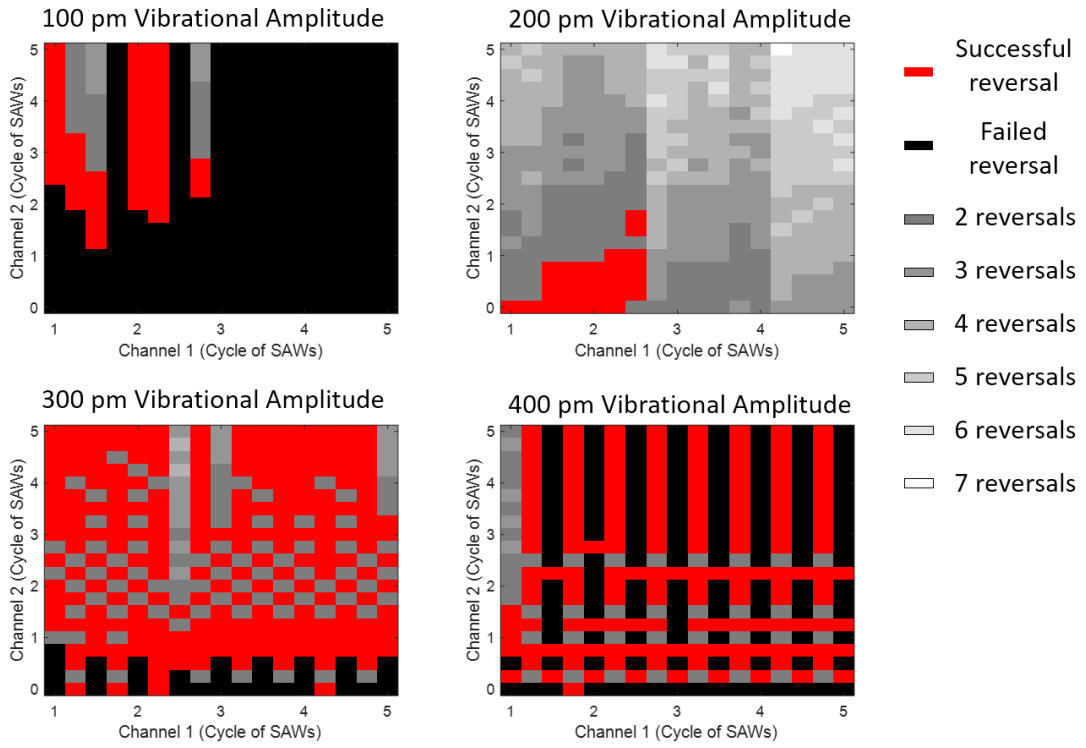

Figure 4.14 Simulation of magnetization reversing with different vibrational amplitude. Channel 1 and 2 represent the duration of 45° SAW burst and -45° acoustic is on.

Each plot in figure 4.14 has 357 cases in total, and the red portion in figure 4.14 is successful reversal, but the black portion is not. However, the gray scale area represents the multi-reversal situation, and the lighter color in figure 4.14, the more times the magnetization reversed. To optimize the switching durations, we classify the cases shown in figure 4.14 in four categories, and we use the margin, saturated magnetization and the first peak of magnetization in x direction, to determine the chance of double reversal:

1. Double reversal: For example, at 400 pm vibrational amplitude with 2.25 cycles for channel 1, and 1 cycle for channel 2 this behavior is seen, and this is depicted in figure 4.15.
2. Reversal with poor margin: For this case magnetization is reversed. However, for this case the dynamics of the magnetization in the final position shows oscillatory behavior and hence this scenario may result in the double reversal due to external interference, such as thermo interference or external fields. For example, at 300 pm vibrational amplitude with 2.25 cycles for duration 1, and 1 cycle for duration 2 we can see this scenario, as shown in figure 4.16.
3. Reversal with good margin: For this case, the magnetization is reversed and the dynamics of the magnetization damps down over time and hence this scenario is optimal as it is robust against external interference. For example, at 100 pm vibrational amplitude with 1.25 cycles for duration 1, and 2.25 cycle for duration 2 this behavior is seen. This scenario is shown in figure 4.17.

4. Failed reversal: For this case, the strain value is not strong enough and the timing is not suitable enough to perform the magnetization switching. This is shown in figure 4.18.

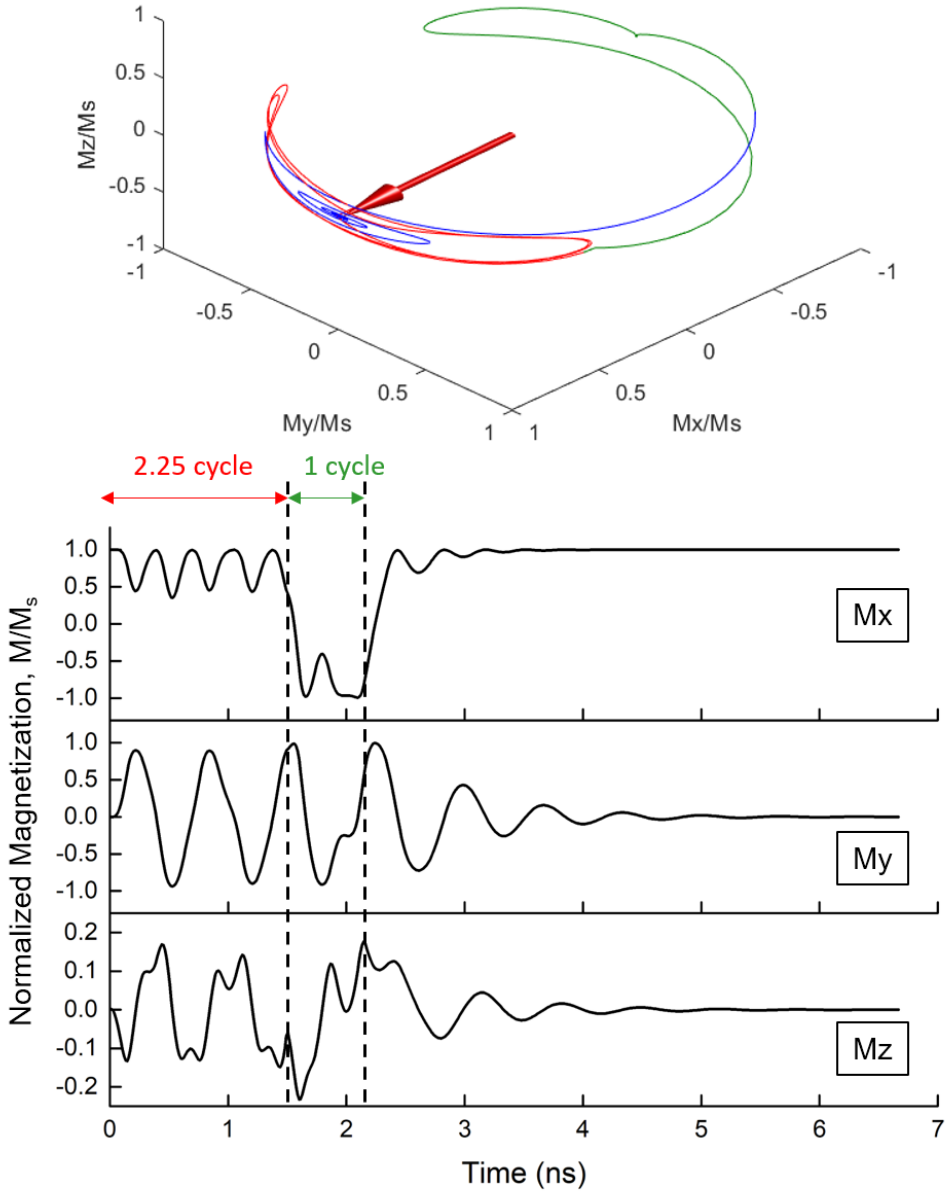

Figure 4.15 Simulation of double reversal of the magnetization direction. The duration of SAW burst is indicated by the colors: duration 1 is red, duration 2 is green, and the rest of time are shown in blue.

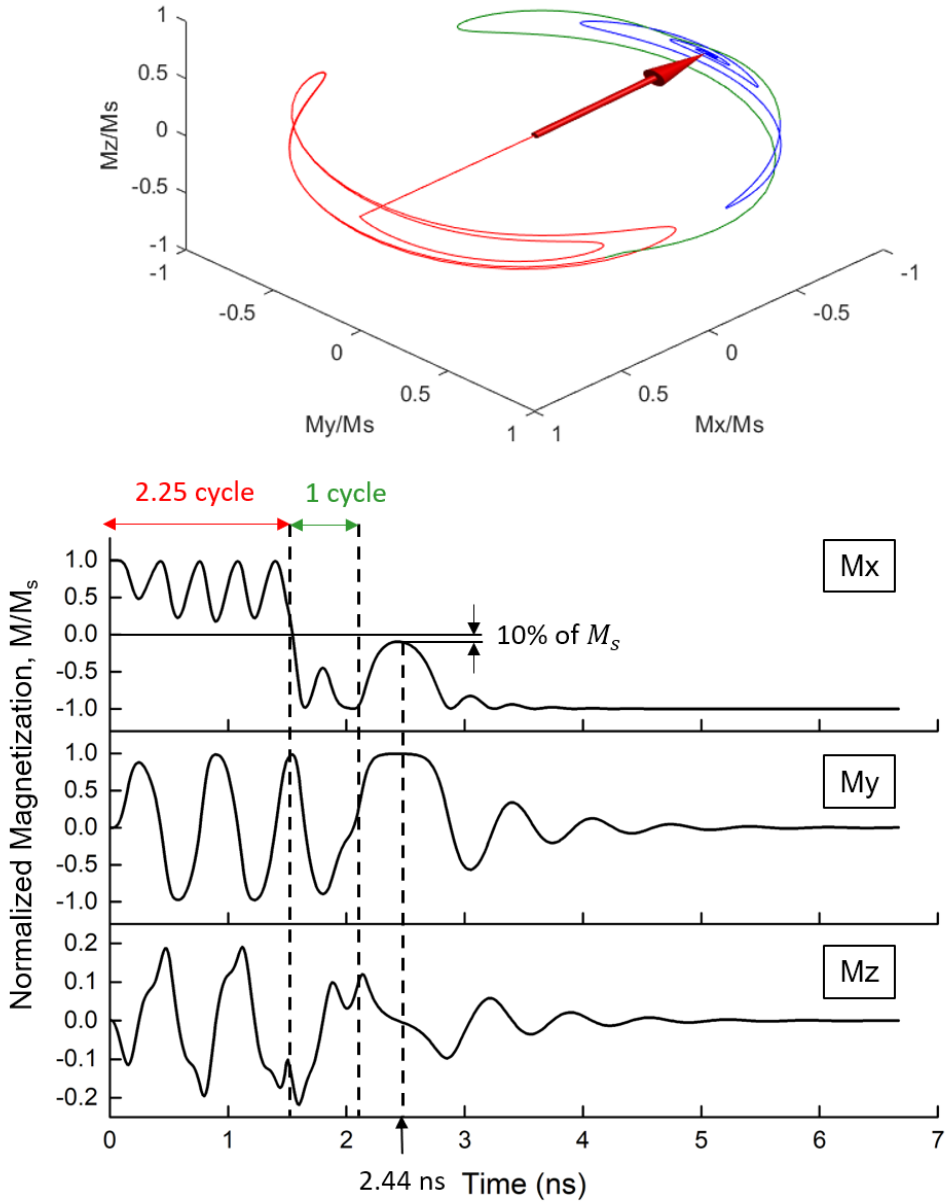

Figure 4.16 Simulation of reversal of the magnetization direction with poor margin driven by 300 pm.

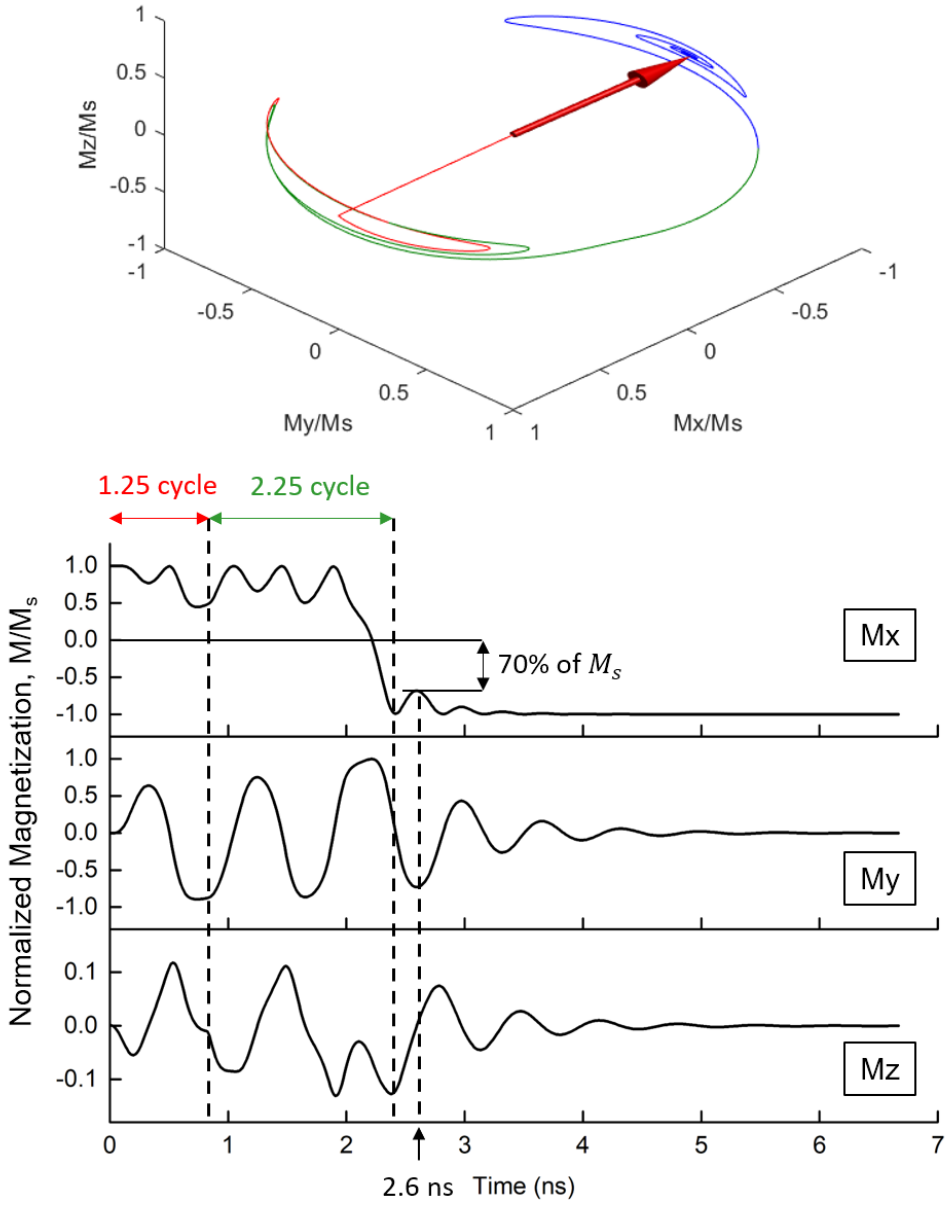

Figure 4.17 Simulation of good margin reversal with 100 pm vibrational amplitude.

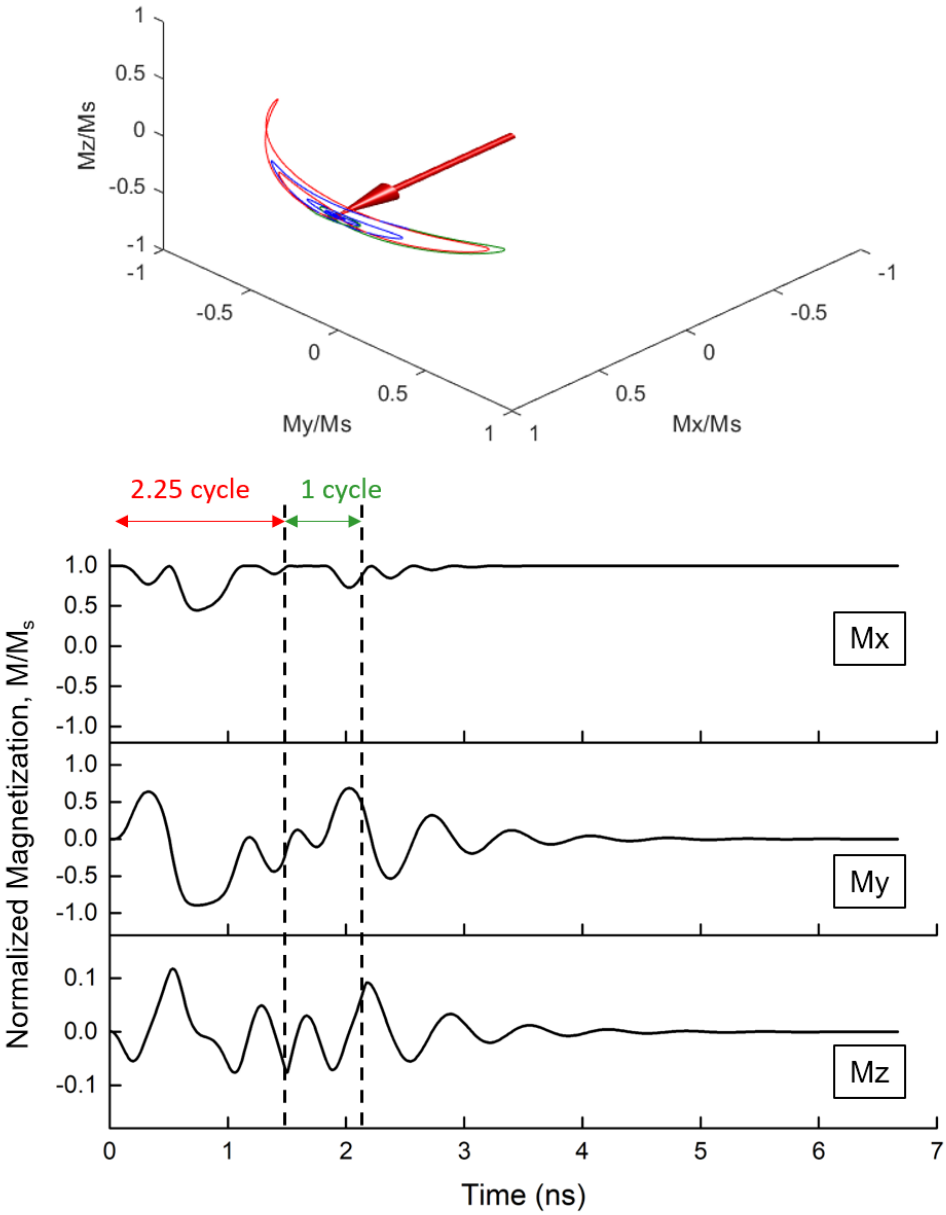

Figure 4.18 Simulation of failed reversal with 100 pm vibrational amplitude.

In figure 4.16 (poor margin reversal), we see that although the magnetization is not over-rotated, the first peak of M_x after 3.25 cycles is close to zero. The M_x in figure 4.15 at 2.44 ns is $-4.5 \times 10^4\ [A/m]$, which is only 10% of the saturation magnetization. Therefore, any external interference may have the chance to over-rotate the magnetization across the hard axis and pull it back to the initial direction. Additionally, some combinations of 100 pm vibrational amplitude also show this behavior. This proves that even with a small vibrational amplitude, it is theoretically possible to accomplish the precessional switching. Figure 4.17 illustrates a damped reversal result with 100 pm vibration amplitude along with 1.25 cycle for duration 1 and 2.25 cycle for duration 2. The M_x in figure 4.17 at 2.6 ns is $-3.2 \times 10^5\ [A/m]$, which is 70% of saturation magnetization. In this case, the probability that the magnetization returns to the initial direction is lower than the case with 300 pm vibrational amplitude case shown in figure 4.16.

In summary, we have applied the experimental results of our acoustic vibration measurement to the MATLAB® simulation and determined the demagnetization factor that has matched FMR frequency to the SAW frequency. According to the simulation results, a strong vibration amplitude may over-rotate the magnetization, and can fail the precessional switching process. On the other hand, the possibility of magnetization switching with low acoustic vibration (such as 100 pm) is also shown in the simulation results. As a result, we have proved the field-free precessional magnetization switching could theoretically be achieved by the FIDT devices that we have developed in this research. In the end, these simulation results provide a map which includes the

amplitude of acoustic vibration, as well as the timing and duration of SAW burst for the future experiment and implementation.

Chapter 5 Discussion and Future Work

In this work, we have proposed a new method that is to reverse the magnetization by using precessional switching driven by SAWs. The main benefit of this technique is that we do not have to apply any external magnetic field, and hence, the coil for generating field does not be needed. For the experimental results we have shown that the FIDTs have successfully focused the SAWs to the focal point. According to these acoustic vibration results, we have provided a map that includes the combination of duration of the SAW bursts for magnetization switching. A device with Ni deposited on the focal spot was fabricated, but the domain structure was not visible on the magneto-optic Kerr effect (MOKE) microscope, and hence, we were not able to proceed with the field-free switching experiment with Ni. On the other hand, we expect galfenol (FeGa) to show the domain structure in MOKE microscope because FeGa has a higher magnetostriction coefficient than Ni; hence FeGa is a suitable choice for our device. However, the implementation could not be completed because of the inability to sputter FeGa on our device. With more time we could have implemented and validated the simulation results experimentally with FeGa. The experimental validation of our simulation can be future research problem. In the present work, we focused on the design of the device, and we have shown that FIDTs can generate enough strain that is required for the field-free switching. In addition to the experimental measurement of the vibrational amplitude, we have simulated the field-free switching theoretically.

Another future research can focus on the shape of the magnetostrictive material as it is also a critical factor in this research. In order to match the SAW frequency to

the FMR frequency of Ni , which is 1.5 GHz, we determined that the ratio of the demagnetization factors (N_x/N_y) must be 0.89 (given the magnetization of Ni), but this ratio being so near to 1 means that the magnetization would be unstable and could be easily reversed by an external magnetic field causing this device to be unusable for magnetic storage. In order to overcome this issue, the SAW frequency may be increased in the future design, such as using fifth or seventh harmonic of our FIDT device in the experiment, in that case the ratio N_x/N_y can be reduced. For example, at fifth harmonic, this ratio is 0.61 for Ni. However, we have already mentioned in chapter 4, that our interferometer will not be able to probe at higher harmonics, and hence the interferometer needs to be redesigned.

Bibliography

[1] J. P. Joule, “XVII. On the effects of magnetism upon the dimensions of iron and steel bars,” *London, Edinburgh, Dublin Philos. Mag. J. Sci.*, vol. 30, no. 199, pp. 76–87, 1847.

[2] H. Rubinstein, R. Hornreich, J. Teixeira, and E. Cohler, “Soniscan: A ferroacoustic thin-film memory,” *IEEE Trans. Magn.*, vol. 6, no. 3, pp. 475–488, 1970.

[3] I. S. Camara, J. Y. Duquesne, A. Lemaître, C. Gourdon, and L. Thevenard, “Field-Free magnetization switching by an acoustic wave,” *Phys. Rev. Appl.*, vol. 11, no. 1, pp. 1–5, 2019.

[4] L. Thevenard *et al.*, “Precessional magnetization switching by a surface acoustic wave,” *Phys. Rev. B*, vol. 93, no. 13, pp. 1–7, 2016.

[5] J. E. Graebner, “Optical scanning interferometer for dynamic imaging of high-frequency surface motion,” *Proc. IEEE Ultrason. Symp.*, vol. 1, pp. 733–736, 2000.

[6] K. Kokkonen, J. V. Knuuttila, V. P. Plessky, and M. M. Salomaa, “Phase-sensitive absolute-amplitude measurements of surface waves using heterodyne interferometry,” *Proc. IEEE Ultrason. Symp.*, vol. 2, no. 2, pp. 1145–1148, 2003.

[7] CrystalLaser, “CrystalLaser CL532-005,” *datasheet*, no. Opensource Online.

[8] F. J. Duarte, *Tunable laser optics*. CRC Press, 2017.

[9] R. Otoole, “NIKON CFI PLAN 10X ACHROMAT OBJECTIVE MRL00102,” 2017. [Online]. Available:

https://www.closeuphotography.com/nikon-cfi-plan-10x-achromat-objective/2017/5/23/nikon-cfi-plan-10x-achromat-objective. [Accessed: 01-Feb-2020].

[10] D. Krstić, *RF microelectronics*, 2nd ed., vol. 29, no. 12. Prentice Hall New Jersey, 1998.

[11] J. B. Green and G. S. Kino, "SAW convolvers using focused interdigital transducers," *ITSU*, vol. 30, pp. 43–50, 1983.

[12] R. E. Brooks and J. Z. Wilcox, "SAW RF spectrum analyzer/channelizer using a focusing, phased array transducer," in *IEEE 1985 Ultrasonics Symposium*, 1985, pp. 91–95.

[13] J. Z. Wilcox and R. E. Brooks, "Time-Fourier transform by a focusing array of phased surface acoustic wave transducers," *J. Appl. Phys.*, vol. 58, no. 3, pp. 1148–1159, 1985.

[14] W. Li, "Acoustically Assisted Magnetic Recording," Oregon State University, 2015.

[15] S. Datta, *Surface acoustic wave devices*. Prentice Hall, 1986.

[16] V. Laude and S. Ballandras, "Slowness curves and characteristics of surface acoustic waves propagating obliquely in periodic finite-thickness electrode gratings," *J. Appl. Phys.*, vol. 94, no. 2, pp. 1235–1242, 2003.

[17] A. A. Maznev, A. M. Lomonosov, P. Hess, and A. A. Kolomenskii, "Anisotropic effects in surface acoustic wave propagation from a point source in a crystal," *Eur. Phys. J. B*, vol. 35, no. 3, pp. 429–439, 2003.

[18] V. Laude, D. Gérard, N. Khelfaoui, C. F. Jerez-Hanckes, S. Benchabane, and

A. Khelif, “Subwavelength focusing of surface acoustic waves generated by an annular interdigital transducer,” *Appl. Phys. Lett.*, vol. 92, no. 9, pp. 1–3, 2008.

[19] M. Anhorn, H. E. Engan, and A. Ronnekleiv, “New SAW velocity measurements on Y-cut $LiNbO_3$.,” *Ultrason. Symp. Proc.*, pp. 279–284, 1987.

[20] H. S. Park, H. S. Lee, H. S. Lee, H. B. Kim, and Y. H. Kim, “Measurement of ultrasonic surface wave velocities in silicon crystals and its comparison with finite element analysis,” *Jpn. J. Appl. Phys.*, vol. 56, no. 7, pp. 3–8, 2017.

[21] G. Bertotti, I. Mayergoyz, C. Serpico, and M. Dimian, “Comparison of analytical solutions of Landau-Lifshitz equation for ‘damping’ and ‘precessional’ switchings,” *J. Appl. Phys.*, vol. 93, no. 10 2, pp. 6811–6813, 2003.

[22] M. D’Aquino, “Nonlinear Magnetization dynamics in thin-films and nanoparticles,” 2004.

[23] R. M. (Richard M.) Bozorth, *Ferromagnetism*. Piscataway, NJ : IEEE Press, 1978.

[24] M. W. Gutowski, “Where is magnetic anisotropy field pointing to?,” *arXiv Prepr. arXiv1312.7130*, pp. 1–3, 2013.

[25] L. D. Landau and E. Lifshi͡ts, *Physique théorique: Électrodynamique des milieux continus*. .

[26] F. Nickel-Properties, “Applications of Commercially Pure Nickel.” Azo Materials. https://www. azom. com/properties. aspx.

[27] A. J. Slobodnik Jr, E. D. Conway, and R. T. Delmonico, “Microwave acoustics handbook. Volume 1A. Surface Wave Velocities.,” 1973.

[28] J. Walowski, M. D. Kaufmann, B. Lenk, C. Hamann, J. McCord, and M. Münzenberg, “Intrinsic and non-local Gilbert damping in polycrystalline nickel studied by Ti: sapphire laser fs spectroscopy,” *J. Phys. D. Appl. Phys.*, vol. 41, no. 16, p. 164016, 2008.

[29] R. C. O’handley, *Modern magnetic materials: principles and applications*. Wiley, 2000.

Appendix A: Focused Interdigital Transducer Layout Design

According to the group velocity of Y-cut $LiNbO_3$ that has been determined in chapter 2, the spacing between FIDT fingers is determined as (v_g/500) μm, and the width of FIDT fingers in this work is the same with their spacing. The focal length of the FIDT is 40 wavelength of SAW in 500 MHz, and the arc of the FIDT is 60°.

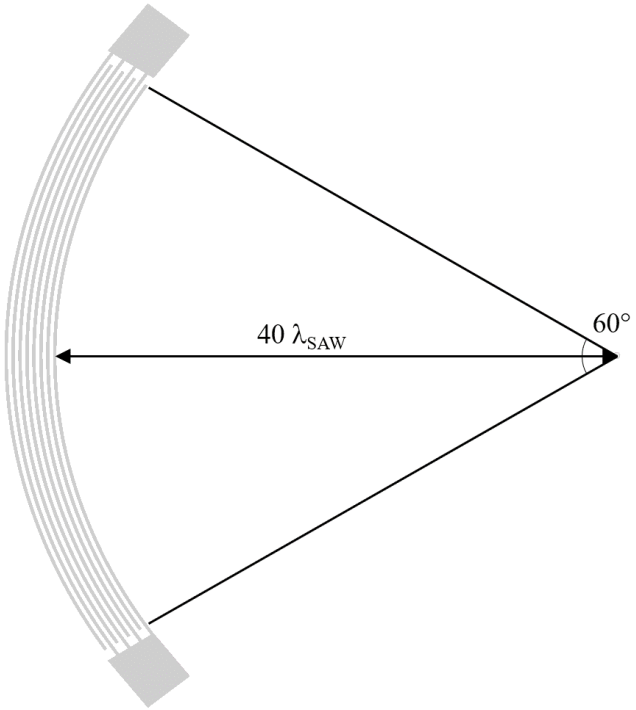

Figure A.1 Layout of the FIDT fingers that have been used in the interferometer measurements.

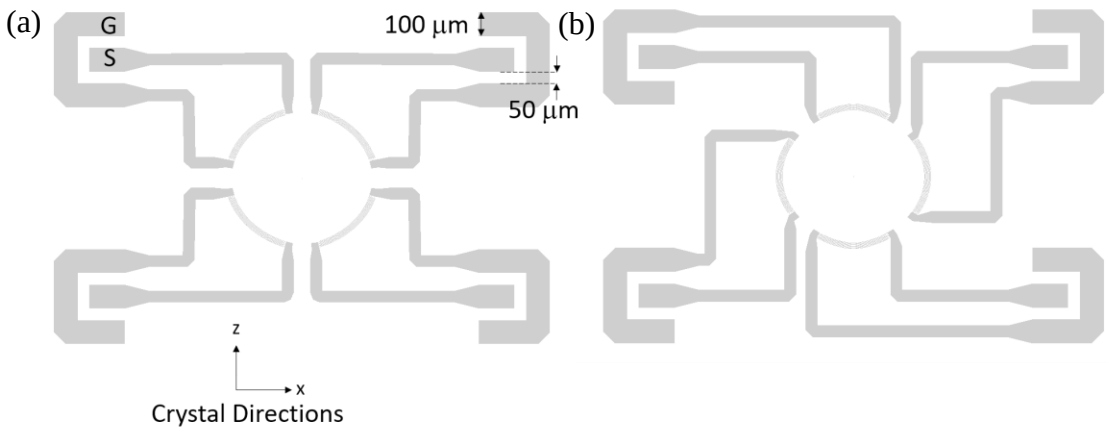

Figure A.2 Layout of FIDT device for measuring frequency response purpose. (a) 4 sets of FIDT fingers with 60° arc and 45° from the x axis. (b) 4 sets of FIDT fingers with 60° arc and 0° and 90° from the x axis.

In figure A.2, the layout of the devices for measuring frequency purpose that have been mentioned in chapter 4 are shown. The design process of these two layouts has been described in previous paragraph. Noted that the semiconductor probe is used for the signal input of the FIDT fingers, and the pads for contacting the probe was made for matching the spacing of the signal and ground port of the semiconductor probe.

The ADS layout files of the FIDT design for this work can be found in the shared drive of Applied Magnetics Laboratory (address: Z:\Data\Han-Ting Lin\FIDT Layouts\LiNbO3_Y-cut_FIDTs).